ELSEVIER

Neoproterozoic basalts of the Paleo-Asian Ocean (Kurai accretionary zone, Gorny Altai, Russia): geochemistry, petrogenesis, and geodynamics

I.Yu. Safonova [a,*], V.A. Simonov [a], M.M. Buslov [a], T. Ota [b], Sh. Maruyama [c]

[a] *Institute of Geology and Mineralogy, Siberian Branch of the RAS, 3 prosp. Akad. Koptyuga, Novosibirsk, 630090, Russia*
[b] *Institute for Study of the Earth's Interior, Okayama University at Misasa, Tottori 682-0193, Japan*
[c] *Tokyo Institute of Technology, 2-12-1 O-okayama, Meguro-ku, Tokyo, 152-8550, Japan*

Abstract

Late Neoproterozoic (Late Vendian) basalts of the Paleo-Asian Ocean are found as fragments incorporated in the Kurai accretionary zone, Gorny Altai, Russia. Detailed study of their geochemistry and relationships with associated sedimentary rocks allowed us to recognize three types of basalts: (1) lavas depleted in REE, Nb and Ti, compositionally similar to N-MORB and associated with thin-bedded oceanic siliceous sediments; (2) basalts of transitional compositions, and (3) basalts enriched in the above elements; basalts of types 2 and 3 are similar to Pacific intraplate basalts and are associated with carbonate "cap" sediments. The N-MORB-type basalts generated from a depleted upper-mantle source, whereas the transitional and enriched ones from a heterogeneous mantle source. Their crystallization temperatures were estimated from the experiments on homogenization of melt microinclusions hosted by clinopyroxene phenocrysts (1160–1190 °C) and from the composition of the latter (1100–1295 °C). The geological, lithological, petrological, and geochemical data show that the Kurai basalts were formed in the geodynamic settings of mid-oceanic ridges and oceanic seamounts/islands.
© 2008, IGM, Siberian Branch of the RAS. Published by Elsevier B.V. All rights reserved.

Keywords: Paleo-Asian Ocean, Gorny Altai, basalts, melt microinclusions, major and trace-element geochemistry, crystallization temperature, MORB, OIB

Introduction

Study of fragments of ancient oceanic lithosphere incorporated in foldbelts is necessary for understanding evolution of formerly existed oceans and processes of continental crust growth during accretion and collision. The fragments of the Paleo-Asian Ocean lithosphere comprising oceanic floor basalts formed within mid-oceanic ridges (N-MORB type) and intraplate basalts of oceanic rises (oceanic islands and plateaus — OIB and OPB, respectively) have been found in many folded structures of the Altai-Sayan Area (ASA) (e.g. Berzin and Kungurtsev, 1996; Buslov and Watanabe, 1996; Buslov et al., 1993, 2001; Dobretsov and Zonenshain, 1985; Dobretsov et al., 1992, 2004, 2005; Kurenkov et al., 2002; Safonova et al., 2004; Simonov, 1993; Simonov et al., 2004).

Many regions of ASA host fragments of the Paleoasian oceanic crust like that of Gorny Altai (Fig. 1), which is an Early Caledonian accretionary structure also comprising fragments of Vendian-Cambrian island arcs (Buslov and Watan-

abe, 1996; Buslov et al., 1993, 2001, 2002; Simonov et al., 1994; Watanabe et al., 1994).

The paper presents criteria for identification of oceanic basalts from the Kurai accretionary complex of Gorny Altai (or Kurai greenstones), parameters of their petrogenesis, types of mantle sources and geodynamic settings of formation based on a complex analysis of structural, lithological, petrological, and geochemical data.

Geological position of basalts

In Gorny Altai oceanic basalts are common within the accretionary prism of the Kuznetsk-Altai island arc, which includes the Kurai accretionary complex or accretionary wedge located in its southwestern part (Fig. 1) (Buslov and Watanabe, 1996; Buslov et al., 2001, 2002; Dobretsov et al., 2004; Ota et al., 2007; Safonova et al., 2004; Uchio et al., 2004). The accretionary units are overlapped by Middle-Late Cambrian sedimentary rocks of the Anui-Chuya fore-arc trough and are exposed over a large territory from Chagan-Uzun to Aktash Village (East-West). The best exposed

* Corresponding author.
  E-mail address: inna@uiggm.nsc.ru (I.Yu. Safonova)
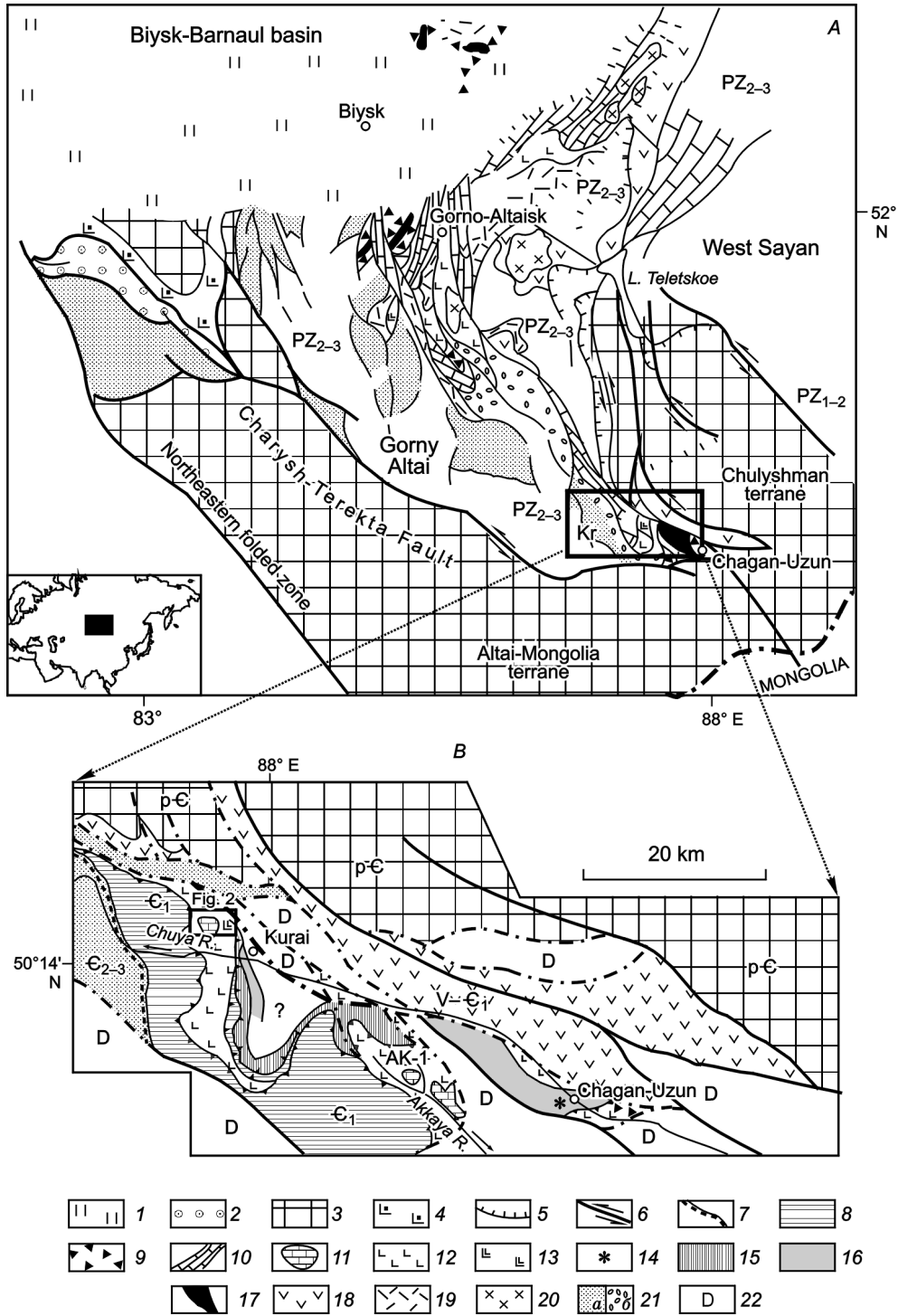
Fig. 1. *A* — Vendian-Cambrian island-arc and oceanic units of Gorny Altai (modified from Buslov et al., 2001). Kr — Kurai accretionary wedge. *B* — Geological scheme of the Kurai accretionary wedge. *1* — Neogene-Quaternary sediments, *2* — Early Ordovician fore-arc basin, *3* — Precambrian terranes, *4* — Late Neoproterozoic-Early Ordovician oceanic crust, *5* — thrust, *6* — strike-slip fault, *7* — Cambrian fault, *8* — stratigraphic contact; *9–17* — Kurai accretionary wedge: *9* — Early Cambrian olistostrome, undivided fragments of MORB, OIB, OPB and exotic "black limestone" units; *10* — olistostrome; *11* — oceanic island carbonate sediments; *12* — Early Cambrian reef limestone and dolomite of the Kurai paleoseamount carbonate "cap"; *13* — OIB/OPB; *14* — N-MORB; *15* — eclogite; *16* — Early Cambrian amphibolite and blueschist; *17* — Late Neoproterozoic-Early Cambrian serpentinite and ophiolite; *18* — Chagan-Uzun gabbro-ultramafic massif; *19–23* — Late Neoproterozoic-Early Cambrian Kuznetsk-Altai island arc: *19* — tholeiite-boninite series, *20* — calc-alkaline series, *21* — gabbro, *22* — Middle-Late Cambrian Anui-Chuya fore-arc basin (*a* — flysch, *b* — olistostrome), *23* — Devonian volcanosedimentary rocks.

localities are near Chagan-Uzun and Kurai Villages (Fig. 1). The Kurai accretionary complex consists of tectonic sheets — fragments of two main units: basaltic and carbonate. Although the rocks of the tectonic sheets have different compositions and were formed in different geodynamic settings, they were traditionally regarded elements of a single stratigraphic section

(Zybin and Sergeev, 1978). The tectonic sheets of the basaltic unit consist of pillow lavas, flows and dikes of pyroxene and plagioclase porphyric and aphyric basalts and diabases and olistostromes referred to the Arydzhan or Sagalak Formation. The carbonate unit is referred to the Baratal Formation and consists of gray limestones with chert lenses and interbeds.

Near Kurai Village the basalts are associated with sedimentary rocks and compose the Baratal oceanic paleoisland (thereinafter — Baratal paleoseamount) (Buslov et al., 2001; Dobretsov et al., 2004). The tectonic sheets of the paleoseamount alternate with olistostromes, peridotites, and serpentinitic melange hosting high-pressure rocks. The sedimentary rocks are typical members of Oceanic Plate Stratigraphy (Isozaki et al., 1990), which is characterized by a regular transition from seamount-top shallow-water reef limestone to hemipelagic slope facies sediments (siliceous mudstone, clastic limestone, etc.) and then to pelagic sediments of seamount foothill and oceanic floor (bedded radiolarian chert). The Late Neoproterozoic age of basalts was estimated by the age of their associated limestones, whose Pb-Pb isochron dating yielded 598±25 Ma (Uchio et al., 2004).

A fragment of the Baratal paleoseamount is exposed north-west of Kurai Village (Fig. 2) and consists of basaltic lavas, dike-sill complex and sedimentary rocks. The paleoseamount is overlapped by island cap limestones and underlain by oceanic floor basalts. The sampling site displays primary relationships between the paleoseamount basalts and carbonate cap/slope facies sediments and between the oceanic floor basalts and sedimentary-volcanogenic rocks of the paleoseamount foothill (Figs. 2, 3) (Buslov et al., 2002; Dobretsov et al., 2004; Uchio et al., 2004). The oceanic floor basalts are pillow lavas and clastic lavas associated with green and gray cherts. The dominating varieties are olivine-pyroxene and pyroxene porphyric basalts, which are in the greenschist facies of metamorphism. Olivine is almost completely replaced by serpentine whereas pyroxene and volcanic glass — by chlorite and epidote.

The rock varieties of the paleoseamount can be divided into volcanogenic, volcanosedimentary and sedimentary units. **The volcanogenic unit** ("main seamount body") consists of pillow lavas of variolitic plagioclase and pyroxene-plagioclase basalts in places containing interbeds and lenses of marble-like limestone and dolomite or, to a lesser degree, siliceous sediments and volcanomictic sandstone.

The volcanosedimentary unit (semipelagic slope facies) consists of bedded and massive limestones, mudstone, pillow
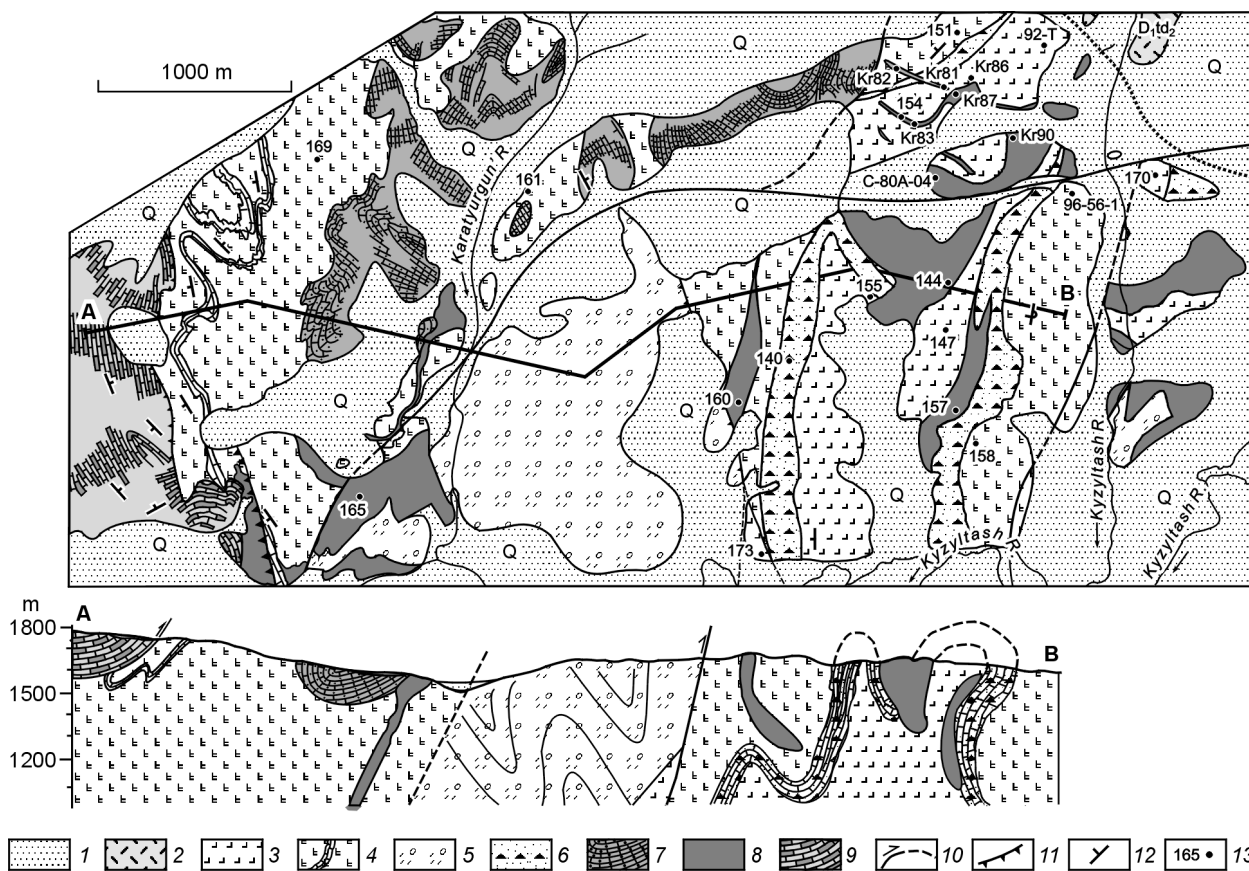
Fig. 2. Detailed geological scheme of the Karatyurgun' site of the Kurai accretionary wedge modified from (Dobretsov et al., 2004). *1* — Quaternary sediments; *2* — Early-Devonian volcanosedimentary rocks; *3* — N-MORB type basalts (?); *4–9* — Late Neoproterozoic rocks of the Baratal paleoseamount: *4* — OPB/OIB volcanogenic unit with limestone beds, *5* — volcanosedimentary slope facies, *6* — volcanogenic, carbonate-siliceous and conglomerate slope facies, *7* — "carbonate cap" massive limestones, *8* — dikes and sills of OPB-type Cpx-porphyric basalts, *9* — Precambrian (?) sulfur-bearing dolomites and limestones; *10* — strike-slip fault; *11* — thrust; *12* — strikes and dips; *13* — sampling localities.
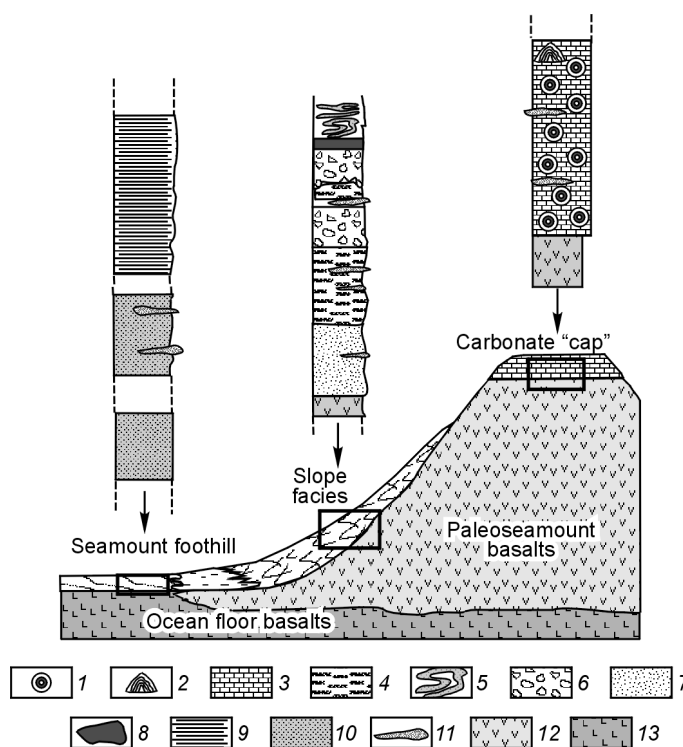
Fig. 3. A schematic reconstruction of the Baratal paleoseamount overlapped by "carbonate cap" sediments (*1–3*), slope facies (*4–8*) and seamount foothill (*9–10*) (modified from (Isozaki et al., 1990)). *1* — ooide, *2* — stromatolite, *3* — massive limestone, *4* — bedded calcareous mudstone, *5* — bedded calcareous mudstone with Z-folds, *6* — clastic sediments/breccia, *7* — poorly sorted calcareous mudstone, *8* — coal seams, *9* — thin-bedded calcareous mudstone, *10* — massive calcareous mudstone, *11* — chert lenses, *12* — seamount basalts, *13* — oceanic floor basalts.

and clastic lavas interbedded with chloritized clayey sediments and volcanomictic sandstones. The sedimentary rocks carry numerous signatures of their formation on volcano slope such as synsedimentary folds (Z-folds) or slump bedding, brecciation and uneven thickness of sedimentary beds. Locally, the volcanosedimentary breccia consists of the clasts of basalt, limestone, mudstone and chert submerged in clay-carbonate-siliceous matrix.

The basalts of the volcanogenic and volcanosedimentary units also have undergone greenschist metamorphism, which resulted in partial or complete replacement of pyroxene and volcanic glass by chlorite and epidote and plagioclase albitization.

The sedimentary unit (carbonate top or "cap" of the paleoseamount) consists of carbonate and siliceous rocks. The carbonate rocks are dominated by gray massive and bedded limestone and carbonate breccia. The limestones rest on the pillow lavas. The massive limestones contain siliceous nodules, lenses of black limestone, stromatolites and ooides. The bedded limestone contains dolomitic material and occurs in association with lime breccia/conglomerate. This association is characterized by slumping structure. The massive gray siliceous rocks (cherts) are intercalated with the bedded limestone (Fig. 3).

The dikes and sills of diabase and gabbro-diabase cut the main magmatic body of the paleoseamoun the slope facies and the massive limestones of the carbonate cap.

The oceanic basalts were sampled near Kurai Village (Fig. 2; Table 1), (samples 140-173, 96-56-1, KR-82/90, C-80A-04 and 92-T-2, 4) and near Chagan-Uzun Village, in the Akkaya River valley (Fig. 1; site AK-1; samples 123, 125).

Analytical methods

Samples for geochemical analyses were obtained from the least altered and deformed outcrops of pillow lavas and flows. All the samples were powdered using an agate mill. Major element oxides were 100±1 wt.%. Most analyses were made at the Institute of Geology and Mineralogy, Siberian Branch, Russian Academy of Science. Abundances of major and trace elements (Rb, Sr, Ba, V, Ni, Zn, Ga, Y, Zr, Nb) were determined by X-ray fluorescence (XRF) using a "Nauchpribor" spectrometer (analytical procedure following the Russian state analytical standard OST-41-08-212-82 Mingeo SSSR) and SR XRF (synchrotron radiation XRF, description of technique see in (Bobrov et al., 1998) and (Phedorin et al., 2000)). Abundances of Sc, Cr, Co, Hf, Ta, Th and rare earth elements were determined by instrumental neutron activation analysis (INAA) using Ge detectors for γ-rays over 30 keV and under 2000 keV.

For verification of obtained INAA and XRF results 29 trace elements (rare earths — REE, high-field strength elements — HFSE, large-ion lithophile elements — LILE) were determined in 3 samples by inductively coupled plasma mass spectrometry (ICP-MS) using a Finnigan mass-spectrometer. The observed discrepancies between INAA/XRF and ICP MS methods respectively were less than 10% for REE and less than 15% for other trace elements.

Selected element ratios are normalized to primitive mantle so that zero fractionation be unity (e.g. primitive mantle $Nb/Th_{pm} = 1$).

The analyses of clinopyroxenes and their melt inclusions were made with a Cameca CAMEBAX electron microprobe running at a beam current of 40 mA and acceleration voltage of 20 kV. The beam width was usually about 2 μm and was defocused for glass blue diopside analyses. The melt inclusions were homogenized in a high-temperature thermochamber in inert medium according to a technique reported in (Simonov, 1993; Sobolev, 1997; Sobolev and Danyushevsky, 1994). Trace element concentrations in the melt inclusions and their hosting clinopyroxenes were determined at the Institute of Microelectronics RAS (Yaroslavl', Russia) with an IMS-4f ionic probe by a technique of Sobolev (1996).

Petrography

The oceanic basalts of the Kurai accretionary complex have diverse petrographic textures, ranging from fine- to medium-grained amygdaloidal and porphyric to aphyric varieties, but

Table 1
Major (wt.%) and trace (ppm) element compositions of oceanic basalts from the Kurai accretionary belt of Gorny Altai

Component	147	170	92-T-2	92-T-4	173	KR86	123	125	144	146	151	154	155	157	161	165	169	KR82	KR83	KR87	KR90	C-80-04	96-56-1
	1	2	3	4	5	6	7	8	9	10	11	12	13	14	15	16	17	18	19	20	21	22	23
SiO_2	49.18	48.51	49.16	48.69	51.75	49.59	51.15	50.84	48.94	47.25	49.63	46.27	52.36	47.28	47.53	47.29	48.89	49.22	48.69	50.76	49.73	48.45	50.15
TiO_2	1.75	1.45	1.10	1.14	0.79	1.02	1.32	1.66	1.77	1.84	1.09	2.36	1.84	1.53	1.78	1.65	0.43	2.05	2.42	2.07	1.68	1.86	1.51
Al_2O_3	13.10	13.44	15.07	15.50	13.90	15.15	13.47	14.83	13.49	13.67	15.80	12.90	14.17	15.72	16.15	14.60	17.86	14.24	14.39	16.36	13.84	12.21	14.57
Fe_2O_3	12.85	14.38	12.12	12.12	11.56	11.91	8.04	7.51	11.73	12.91	11.34	14.96	11.24	10.93	12.33	13.57	8.82	13.39	14.53	11.61	11.81	11.73	13.76
MnO	0.24	0.24	0.14	0.15	0.21	0.22	0.16	0.17	0.21	0.23	0.20	0.25	0.17	0.21	0.21	0.21	0.18	0.21	0.24	0.21	0.45	0.18	0.26
MgO	6.94	5.92	5.78	6.09	7.65	5.27	7.87	5.43	7.23	7.26	6.24	6.96	4.59	7.07	7.25	6.69	6.23	6.05	4.91	4.35	6.04	7.73	3.89
CaO	8.67	6.37	9.97	9.44	6.64	9.09	8.71	7.34	9.30	10.00	7.76	6.82	6.32	8.11	5.24	6.95	8.06	8.79	7.47	8.07	8.30	10.97	5.44
Na_2O	4.23	6.21	2.74	3.06	3.88	5.15	3.04	4.58	3.86	3.32	3.28	5.18	4.76	3.85	4.44	4.28	4.75	3.92	3.88	5.00	5.27	2.09	5.76
K_2O	0.36	0.21	0.10	0.10	0.76	0.03	1.34	0.71	0.35	0.29	0.37	0.49	0.70	0.74	0.44	0.44	0.90	0.21	1.45	0.45	0.12	0.30	0.71
P_2O_5	0.18	0.10	0.12	0.11	0.05	0.10	0.17	0.45	0.18	0.18	0.08	0.23	0.21	0.13	0.43	0.37	0.40	0.23	0.25	0.25	0.18	1.18	0.58
LOI	2.37	3.07	4.15	3.92	2.73		4.57	6.10	2.44	2.74	3.83	3.35	2.53	3.19	3.71	3.59	3.13	—	—	—	—	3.98	3.26
Total	99.87	99.90	100.44	100.32	99.91	97.52	99.84	99.62	99.49	99.68	99.62	99.78	98.89	98.75	99.51	99.63	99.65	98.31	98.24	99.12	97.43	100.68	99.89
Mg#	51.93	45.16	48.82	50.12	56.96	46.97	66.19	59.12	55.21	52.93	52.39	48.20	44.96	56.40	54.04	49.65	58.55	47.47	40.34	42.83	50.56	54.26	36.12
La	2.70	3.20	2.80	2.50	3.20	1.86	7.00	8.00	5.30	5.70	7.00	6.50	5.90	7.50	8.00	7.20	20.00	6.08	5.40	6.59	4.51	13.00	11.00
Ce	7.2	8.5	6.0	6.0	8.0	5.54	16.5	18.0	16.0	16.5	20.0	15.5	18.5	18.6	20.6	16.6	42.0	19.05	16.15	20.44	13.76	31.00	25.00
Nd	5.80	6.80	6.20	8.00	6.30	0.99	10.20	14.00	14.90	13.20	14.10	12.30	17.90	10.30	15.60	11.40	19.90	3.26	2.74	3.50	2.39	14.00	16.00
Sm	1.90	2.65	2.20	2.40	1.93	5.56	2.70	4.30	5.05	4.40	4.90	4.70	5.94	3.62	4.20	3.60	4.10	17.35	14.63	18.37	12.83	4.78	5.20
Eu	0.74	1.00	1.10	1.15	0.65	0.85	0.90	1.60	1.70	1.70	1.80	1.65	1.75	1.80	1.88	1.77	1.30	2.04	1.82	1.97	1.50	1.40	2.00
Gd	—	—	3.00	3.80	2.50	8.17	—	—	6.90	—	—	—	—	—	—	—	—	7.97	6.48	3.05	6.10	5.40	—
Tb	0.48	0.57	0.58	0.65	0.71	0.56	0.48	0.95	1.28	1.09	1.06	0.94	1.11	0.74	0.80	0.74	0.41	1.44	1.14	1.47	1.11	0.83	1.10
Yb	2.10	2.70	2.70	2.50	2.20	2.38	2.00	2.80	5.10	5.00	5.00	3.40	4.70	2.70	2.90	2.80	1.40	5.97	4.12	6.20	4.48	1.90	3.80
Lu	0.33	0.48	0.42	0.48	0.32	2.38	0.33	0.41	0.73	0.80	0.80	0.60	0.77	0.40	0.43	0.41	0.22	0.90	0.62	0.93	0.68	0.25	0.55
Cr	165	24.9	—	—	—	—	154	12.5	—	106	113	61	29.2	33.9	38.9	41.7	47.5	—	—	—	—	226.3	—
Co	47	51	—	—	51	—	42	30	55	53	48	52	38	38	39	40	24	—	—	—	—	62	48
Ni	71	9.1	—	—	20	20	96	7.4	51	41	38.9	21.7	22.9	7	22.2	14.3	7.7	39	14	23	42	105.0	—
V	166	341	—	—	—	—	89	135	—	326	362	417	337	307	469	349	67	—	—	—	—	—	—
Rb	3.0	2.8	—	—	12.6	0.5	10.4	11.4	2.8	3.1	7.9	5.5	6.8	6.3	6.5	5.8	19.0	3.4	10.2	4.4	1.5	6.5	15.0
Sr	256	201	—	—	378.2	81.4	315.0	405.0	245.8	211	368	148	171	327	475	514	901	189	125	361	252	161	560
Ba	50	10	—	—	265	26.3	200	270	50	10	160	70	100	260	600	70	300	57	160	177	98	141	480
Ta	0.11	—	0.12	0.10	0.12	0.02	0.53	0.17	0.34	0.22	0.22	0.23	0.20	0.21	0.21	0.16	0.10	0.15	0.16	0.17	0.10	1.23	0.25
Nb	2.0	1.0	—	—	1.4	0.4	9.9	3.0	4.7	4.0	4.2	5.1	4.5	3.7	4.3	3.1	4.1	3.0	3.3	3.3	1.8	20.0	4.0
Zr	58	73	—	—	52	43	96	69	157	157	177	137	186	78	99	72	40.4	173	133	189	132	157.0	108
Hf	1.3	1.6	1.6	1.3	1.5	1.2	2	2.1	4	3.6	3.9	2.9	3.9	1.9	2.1	1.6	0.8	4.5	3.5	5	3.6	3.8	2

Table 1 (continued)

Component	147	170	92-T-2	92-T-4	173	KR86	123	125	144	146	151	154	155	157	161	165	169	KR82	KR83	KR87	KR90	C-80-04	96-56-1
	1	2	3	4	5	6	7	8	9	10	11	12	13	14	15	16	17	18	19	20	21	22	23
Th	0.5	0.18	0.2	0.15	0.35	0.8	0.55	0.5	0.31	0.25	0.3	0.35	0.25	0.45	0.5	0.4	0.85	0.3	0.3	0.5	0.7	1.11	0.9
Y	26.7	35.5	—	—	22	19	22.9	29.9	53	58	63	48.8	61	35.2	38.2	32.6	16	37	50	48	42	42.5	40
U	0.3	0.04	—	—	0.19	—	0.27	0.24	0.19	0.2	0.32	0.05	0.04	0.2	0.28	0.13	0.04	—	—	—	—	0.38	—
Zr/Nb	30	72	—	—	39	121	10	23	33	39	42	27	41	21	23	24	10	58	40	58	74	8	27
La/Sm_N	0.89	0.76	0.80	0.66	1.04	0.57	1.63	1.17	0.66	0.82	0.90	0.87	0.81	1.10	1.20	1.26	3.07	0.67	0.72	0.69	0.64	1.67	1.33
Gd/Yb_N	0.98*	0.95*	0.90	1.08	0.23	0.98	1.17	1.52	1.08	0.94	0.96	1.28	1.02*	1.35*	1.30*	1.21*	1.88	1.03	1.20	1.03	1.06	1.07	1.31*
La/Yb_N	0.87	0.80	0.70	0.68	0.98	0.53	2.37	1.93	0.71	0.77	0.95	1.29	0.85	1.88	1.86	1.74	9.65	0.69	0.89	0.72	0.68	1.69	—
Nb/La_{pm}	0.70	0.30	—	—	0.45	0.62	1.36	0.37	0.85	0.68	0.58	0.75	0.74	0.47	0.52	0.41	0.20	0.47	0.59	0.47	0.38	1.48	0.35
Th/La_{pm}	1.50	0.45	—	—	0.88	3.47	0.64	0.51	0.47	0.35	0.35	0.44	0.34	0.48	0.51	0.45	0.34	0.40	0.45	0.61	1.25	0.69	0.66
Nb/Th_{pm}	0.47	0.67	—	—	0.51	0.18	2.14	0.72	1.81	1.93	1.68	1.72	2.16	0.97	1.03	0.91	0.57	1.19	1.31	0.77	0.30	2.15	0.53
Eu/Eu*	1.03	1.05	1.31	1.24	0.77	1.08	0.98	1.03	3.18	1.03	1.02	1.00	1.02	1.24	1.29	1.39	1.05	0.94	1.03	0.87	0.90	0.81	1.08
Ti/Ti*	4.90	3.06	2.61	2.47	1.91	2.59	2.91	2.14	3.74	2.24	2.15	2.88	2.16	2.15	2.47	2.60	0.72	1.91	2.76	1.84	2.03	2.22	1.64

Note. Eu/Eu* and Ti/Ti* are calculated following the method of Taylor and McLennan (1985) but referenced to Gd and Sm; Gd/Yb$_N$ ratios with star (*) are calculated with the reference to Gd* model value. Ti* — model value extrapolated on the primitive mantle-normalized trace element diagrams. The analyzed material was whole rock powders. Basalts: 1–6 — depleted, 7–21 — transitional, 22–23 — enriched.

the porphyric lavas are predominant. The amygdules are filled with calcite and chlorite. The phenocrysts are plagioclase and clinopyroxene. The clinopyroxene phenocrysts are 0.3–1.0 mm in diameter, colorless, with no pleochroism. Olivine, pyroxene and volcanic glass are partly or completely replaced by chlorite and epidote, and plagioclase — by albite.

Groundmass is variolitic or hyalopilitic. Although the lavas are greenschist facies metamorphosed and contain abundant secondary minerals such as epidote, chlorite and albite, they have well-preserved original igneous textures. Oxide minerals, principally magnetite, are present as accessory phases.

Major and trace element geochemistry

Major and trace element data for Kurai paleoseamount lavas are given in Table 1. The Kurai samples are subalkaline basalts according to their Nb/Y-SiO$_2$ ratios (Winchester and Floyd, 1977) (Fig. 4, *A*) or high-Fe tholeiites according to the Al$_2$O$_3$–TiO$_2$+FeO–MgO triangle classification of Jensen (1976; Fig. 4, *B*). In the present paper they will be referred to as Fe-Mg-tholeiites.

The Mg- to Fe-tholeiitic basalts are characterized by a relatively large range of Mg# and Fe$_2$O$_3$ contents over a restricted range of SiO$_2$: SiO$_2$ spans 44–52 wt.%, Mg# = 66–36 (MgO = 5–7.9 wt.%.), Fe$_2$O$_3$ = 7.5–14.9 wt.%, and Ni = 7–96 ppm. Concentrations of TiO$_2$ and P$_2$O$_5$ range from 0.43 to 2.42 wt.% and from 0.08 to 0.58 wt.%, respectively (Table 1). The ratio of P$_2$O$_5$/TiO$_2$ is over 0.15 in samples 125, 161, 165, 169, 96-56-1 and under 0.15 in the others. Compared to island-arc tholeiites (IAT) (Frolova and Burikova, 1997) the Kurai basalts are characterized by lower K, Rb, Ba and higher Zr, Nb, U, Th, Hf.

FeO* increases so as FeO*/MgO suggesting a tholeiitic trend (Fig. 5, *A*), whereas the increase of TiO$_2$ with growing FeO*/MgO is not so obvious. Therefore in the Miyashiro (1987) diagram the basalts plot between oceanic and island-arc tholeiites (Fig. 5, *B*). Widely varying Ba/Rb (2 to 104 ppm) suggests change of initial concentrations of those mobile alkaline metals during secondary processes. LOI in most samples is less 2 wt.% (Table 1).

In the Kurai accretionary sequence Ti-depleted (1 < TiO$_2$ < 1.3 wt.%) and Ti-undepleted (2.5 > TiO$_2$ > 1.5 wt.%) basalts coexist (Figs. 5, *B*, 6). SiO$_2$ shows negative and CaO positive correlation with respect to MgO (for the Ti-depleted group) (Fig. 6). No clear correlative trends can be found in the variation diagrams of MgO versus trace elements (Fig. 7).

Based on the concentrations of HFSE, LILE, REE and Zr/Nb ratios we divided the Kurai greenstones into three groups. The first group (depleted) includes lavas — N-MORB type tholeiites — characterized by low LREE, LILE and HFSE and increased Zr/Nb (65 in average) (Table 1, nos. 1–6). The dominating second group includes lavas of transitional composition similar to that of oceanic plateau basalts (OPB) with Zr/Nb = 35 in average (Table 1, nos. 7–21). The two samples of the third group (enriched) have OIB-type geochemical affinities and are characterized by increased LILE, LREE,
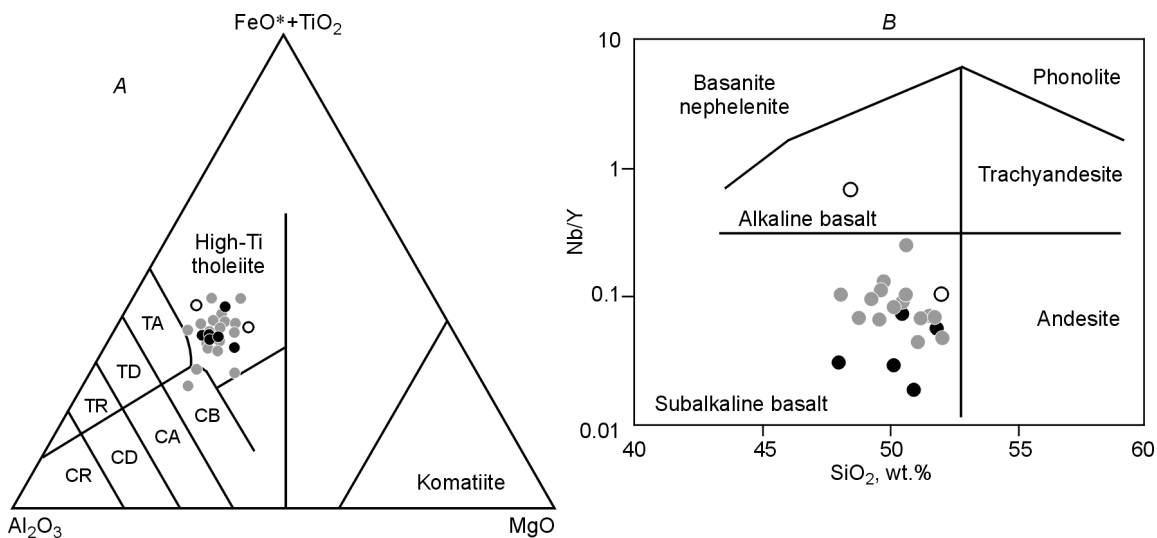
Fig. 4. Classification diagrams for basalts of the Kurai accretionary belt: A — Al_2O_3–FeO^*+TiO_2–MgO diagram (Jensen, 1976); tholeiitic series: TA — andesite, TD — dacite, TR — rhyolite; calc-alkaline series: CB — basalt, CA — andesite, CD — dacite, CR — rhyolite. B — Nb/Y–SiO_2 diagram (Winchester and Floyd, 1977). Symbols for basalts (circles): dark — depleted, open — enriched, gray — transitional.
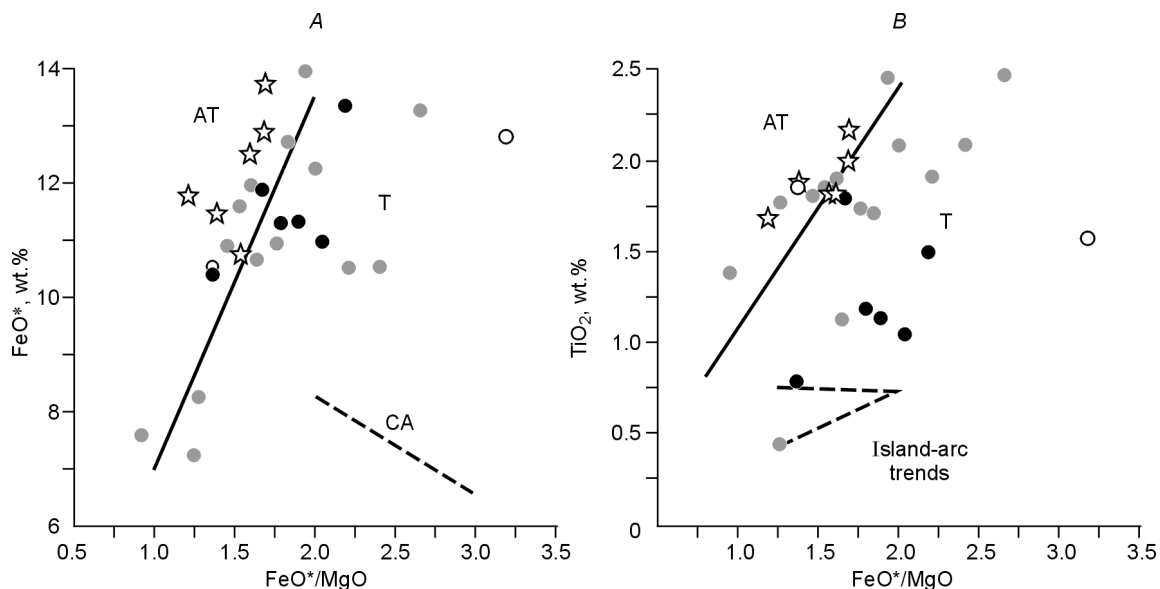
Fig. 5. Bivariant plots: A — FeO^* vs FeO^*/MgO; B — TiO_2^* vs FeO^*/MgO. Discriminant fields and trends of abyssal tholeiite (AT), tholeiite (T) and calc-alkaline volcanic rocks (CA) are after Miyashiro (1973). Stars — clinopyroxene-hosted melt microinclusions; other symbols see in Fig. 4.

HFSE, and low Zr/Nb — 8 and 26, respectively (Table 1, nos. 22–23).

The first group lavas have LREE-depleted rare-earth patterns (Fig. 8, A) with weak positive Eu anomalies: La_N = 5.08–8.7, La/Yb_N = 0.53–0.87, La/Sm_N = 0.57–0.89, Gd/Yb_N = 0.9–1.08 (Table 1). The OPB-type lavas have nearly flat REE patterns (Fig. 8, B), generally higher level of REE concentrations, less fractionated LREE (La/Yb_N < 10): La_N = 12.3–21.8, La/Yb_N = 0.74–2.37, La/Sm_N = 0.7–1.63, Gd/Yb_N = 0.92–1.56 (Table 1). The REE patterns of the Kurai OPB-type lavas are similar to those of the Nauru Basin and Ontong-Java plateau basalts (Safonova et al., 2004). The OIB-type lavas (3rd group) are characterized by higher LREE and medium HREE at La_N = 30–36.8 and $(La/Yb)_N$ = 1.96–4.8. The lavas have moder-

ately LREE enriched REE patterns without Eu anomalies: La/Sm_N ranges from 1.33 to 1.67, and Gd/Yb_N — from 1.07 to 1.31 (Fig. 8, C; Table 1).

The most of primitive mantle normalized trace element diagrams are characterized by negative Nb anomalies and HFSE-REE enrichment relative to MORB (Fig. 9, A). Similarly to the REE patterns the multicomponent spectra of the depleted lavas plot below the spectra of the transitional and enriched lavas. Although Th–Nb–La interelement relationships support the subdivision of the Kurai lavas into three groups, most samples of all groups have moderately depleted Nb and Th concentrations relative to La (Nb/La_{pm} = 0.3–0.75; Th/La_{pm} = 0.3–0.9; Table 1). This is inconsistent with continental rift or plateau basalts, where interaction with older
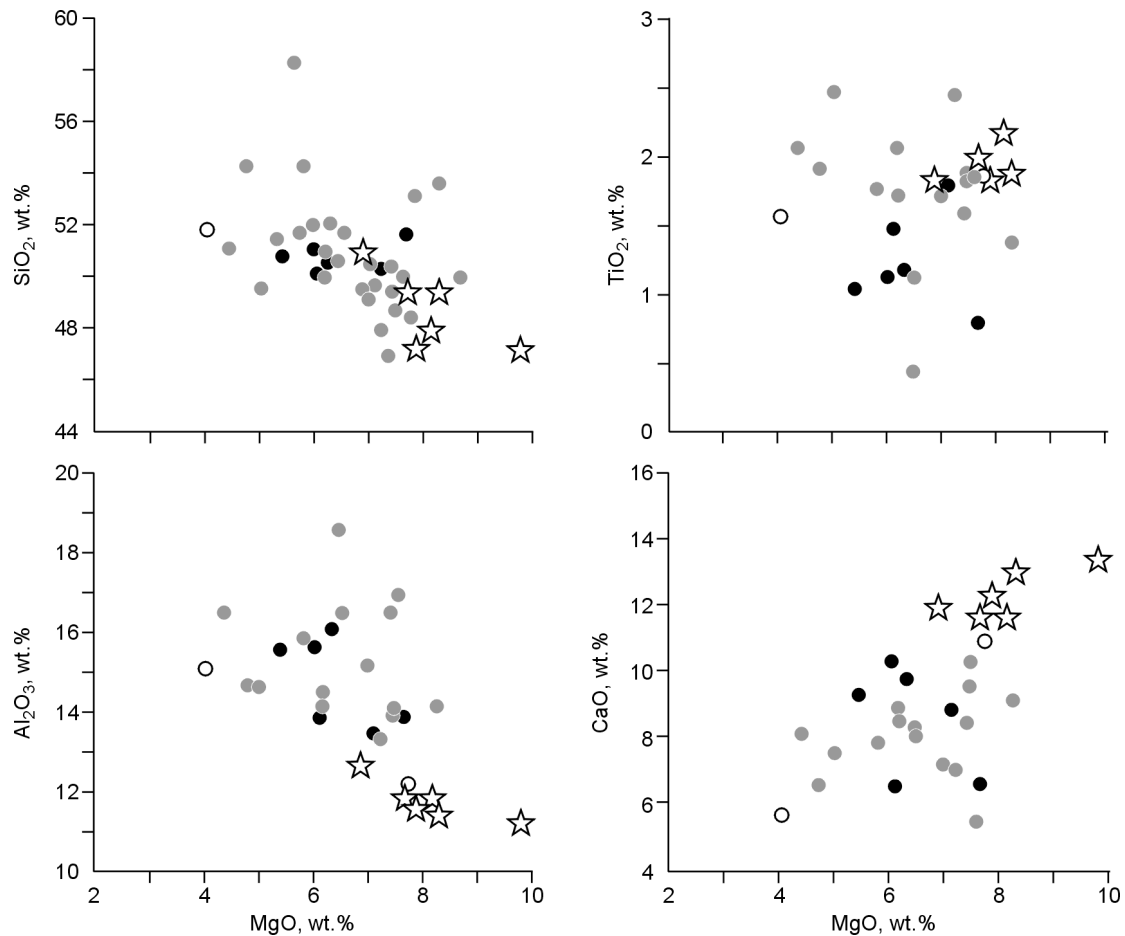
Fig. 6. Variation diagrams of major elements vs. MgO. Symbols as in Fig. 4.

sialic crustal basement often result in Th enrichment, or oceanic island basalts characterized by clear enrichment in Nb. The weakly to zero fractionation of HREE in the Kurai lavas is likely a spinel facies signature of their mantle source.

Clinopyroxene phenocrysts

Table 1 shows the composition of relict igneous clinopyroxenes (Cpx), which occur in basalt sample C-80A-04 (sampling locality see in Fig. 2). The Cpx phenocrysts contain melt microinclusions and mineralogically are $Wo_{37.4-43.3}$ $En_{46.1-49.2}Fs_{8.7-13.6}$, where Wo — wollastonite; En — enstatite; Fs — ferrosilite. In Fig. 10, *A* the Cpx compositions plot between the 1100 and 900 °C isotherms of crystallization (Lindsley, 1983), which is slightly below the temperature ranges of 1100–1295 °C and 1008–1126 °C, as calculated according to the Mercier and Nimis-Taylor pyroxene thermometers (Mercier, 1981; Nimis and Taylor, 2000).

It is commonly accepted that in basaltic rock Cpx composition is controlled by composition of initial magmatic melts, therefore it can be used to deduce the host magma composition (Nisbet and Pearce, 1977). The Al versus Ti diagram (p.f.u.) (Fig. 10, *B*) shows the compositions of Cpx from Kural lavas

compared with Cpx compositions in modern OIB and MORB. At high Al values clinopyroxenes in OIB and MORB have clearly different compositions, and such a tendency has been reported for much older rocks of the Middle Archean Pilbara Craton and Western Australia (Komiya et al., 2002). Compared to modern OIB and MORB, Cpx's from older Kurai lavas are enriched in Ti and depleted in Al (Fig. 10, *B–D*). In the Mg# versus Ti/Al plot (Fig. 10, *C*) Kurai Cpx compositions form a compact field at Mg# = 77–84. Ti/Al ratios of Cpx in Kurai lavas (0.15–0.2) are higher than in modern N-MORB (0.5–1.0), but similar to those in modern and old OIB (Komiya et al., 2002, and references therein). Figure 10, *D* shows that Cpx from Neoproterozoic Kurai lavas contain less Al, Ti and Na at similar Mg# compared to Cenozoic OIB. Cpx in Kurai lavas forms clear magmatic trends in relative to Na and Ti, but no Al trend because of the low Al contents in Cpx.

The analyzed Cpx's have low abundances of LREE (La_N = 0.8–2; La/Yb_N = 0.1) (Fig. 8, *D*); MREE are less depleted relative to HREE, than LREE: La/Sm_N = 0.09–0.13, Gd/Yb_N = 1.4–1.8. Compared with Archean MORB and OIB type basalts of the Pilbara Craton the level of REE concentrations and REE differentiation in Kurai clinopyroxenes is closer to that of the OIB-type (not shown in Fig. 8, *D*) (Komiya et al., 2002). Clinopyroxenes from both Archean and Vendian basalts are
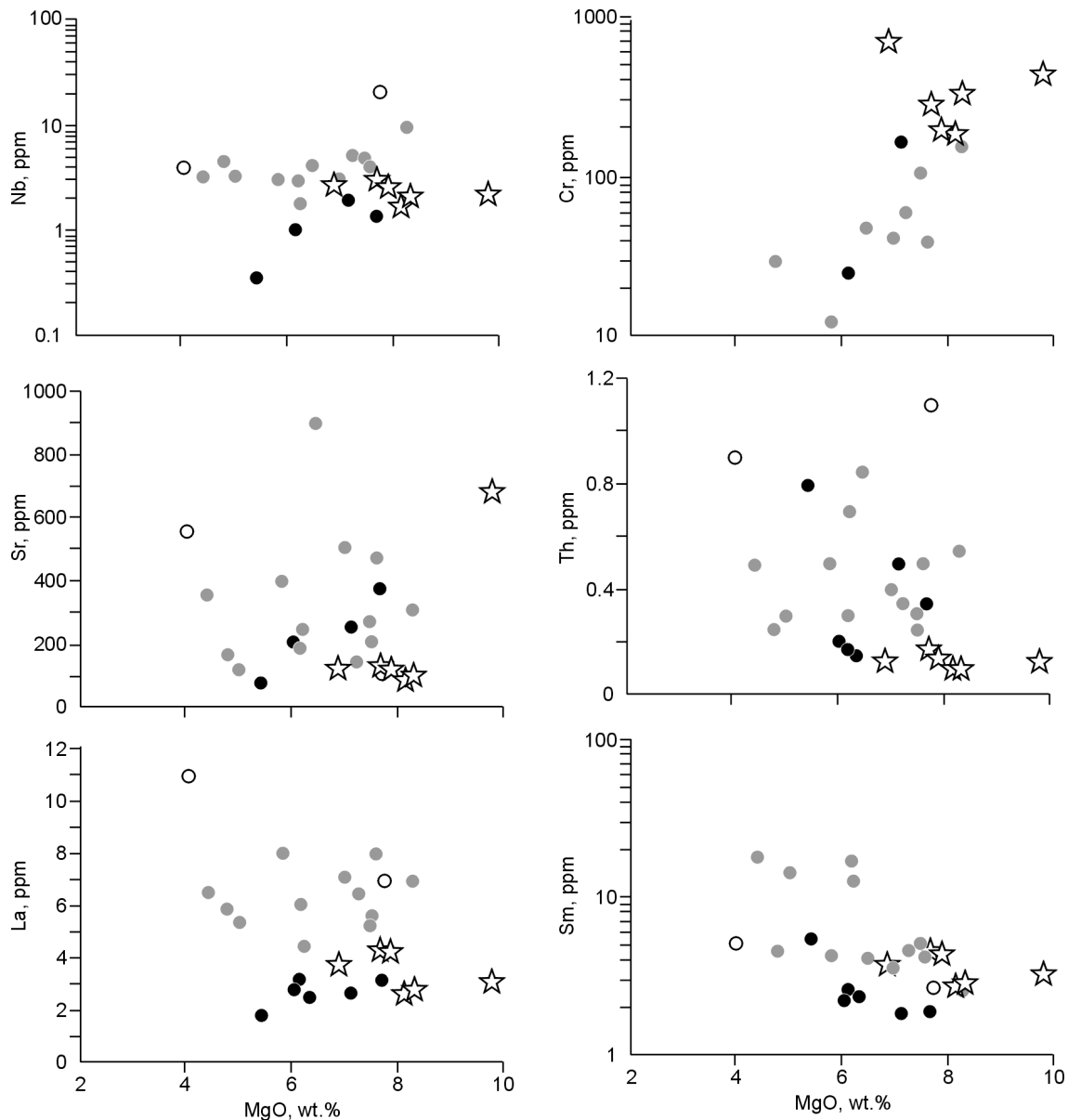
Fig. 7. Variation diagrams of Cr, Sr, Nb, La, Sm and Th vs. MgO. Symbols as in Fig. 4.

characterized by weakly differentiated HREE and La_N ranging from 1 to 3 (Fig. 8, *D*).

Clinopyroxene-hosted melt microinclusions

We studied compositions of melt microinclusions (MIs) in clinopyroxenes of porphyric basalt C-80A-04 (Table 1; Fig. 2). Heating experiments have been carried out in a heating microchamber at temperatures exceeding 1000 °C. After quenching the homogenized MIs were analyzed with a microprobe (Figs. 5–9). The total amount of 60 microprobe analyses of MIs has been first obtained for such an old paleooceanic basalt/greenstone unit. The studied MIs are multiphase, range from 5 to 75 μm in size, and consist of light silicate glass, gas bubble, and daughter crystals (usually greenish solid phase or Fe/Ti oxides). While heated in the heat-chamber the light glass phases become dark at 900 °C; the first portions of light melt and the gas bubble start to separate at 950 °C. MIs homogenization temperatures range from 1160 to 1190 °C.

The MIs show increased TiO_2 (1.1–2.3 wt.%) and on the FeO*/MgO–TiO_2 diagram they plot between three main fields of MORB, OIB and OJB (Fig. 11, *A*). Similarly to Nauru and Ontong-Java lavas the Kurai MIs show a broad range for FeO*/MgO with increasing TiO_2. The MIs show higher average FeO*/MgO compared to MORB and slightly lower TiO_2 compared to OIB suggesting their relation to hot spots (Simonov et al., 2005).

In Fig. 5, *A* the MIs plot close to transitional basalts, however showing higher degree of differentiation compared to both depleted and enriched basalts. In Fig. 6 the MIs plot
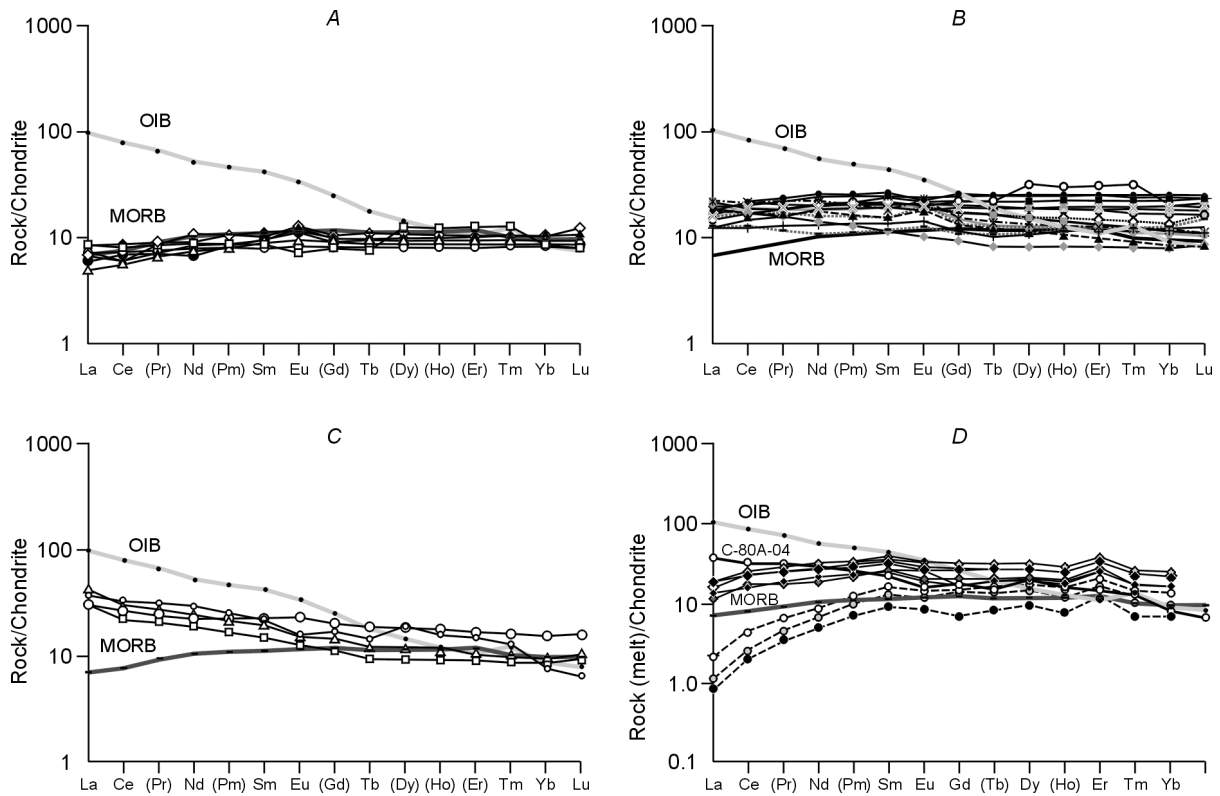
Fig. 8. Chondrite-normalized rare-earth element patterns: *A* — depleted, *B* — transitional, *C* — enriched, *D* — melt microinclusions. The normalizing values are from (Sun and McDonough, 1989).
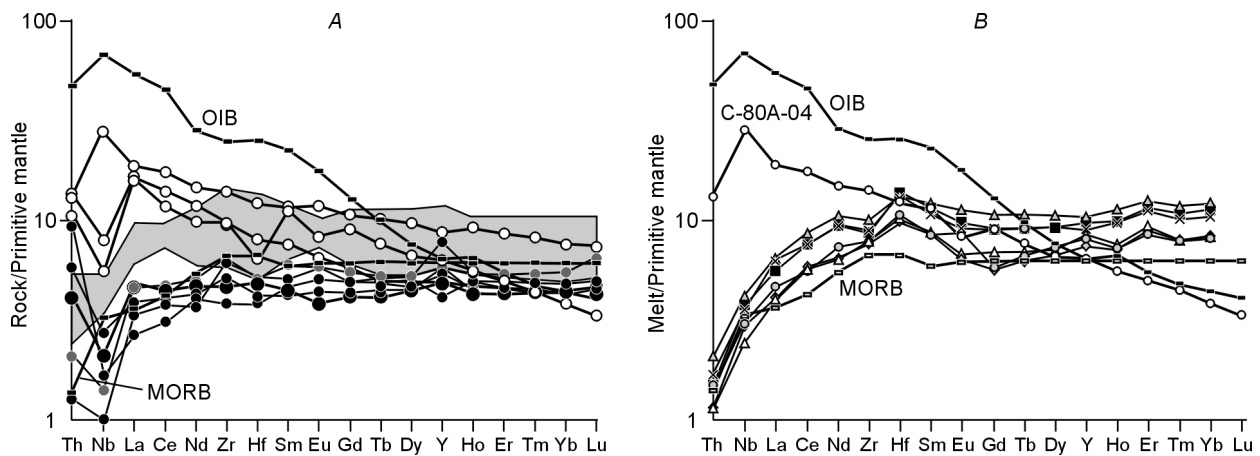
Fig. 9. Primitive mantle-normalized trace element diagrams. *A* — dark and open circles — depleted and enriched basalts, respectively; gray field — transitional ones), *B* — clinopyroxene-hosted melt microinclusions from enriched basalt C-80A-04. The normalizing values, MORB and OIB are from (Sun and McDonough, 1989).

at the end of all differentiation trends and show decreased Al_2O_3 and increased CaO and MgO.

In general, MIs trace-element geochemistry is characterized by higher Cr, lower Sr, Th and Nb/Y and flatter REE patterns than the host basalt C-80A-04 (Table 1, no. 22; Fig. 8, *B*, *D*). The MIs show $La_N = 11.5–18.5$; $La/Yb_N = 0.61–0.76$; $La/Sm_N = 0.46–0.59$; $Gd/Yb_N = 1.95–2.06$: their REE patterns resemble those of Nauru and Ontong-Java plateau basalts and show similar to OPB values of Zr/Nb — 41.2 and 34.6, respectively (Safonova et al., 2004; Simonov et al., 2004). Unlike the host basalt MIs, primitive mantle-normalized trace element dia-

grams lack positive Nb anomaly (Fig. 9). The MIs show Nb depletion relative to La ($Nb/La_{pm} = 0.56–0.72$) and enrichment relative to Th ($Nb/Th_{pm} = 1.98–2.54$).

The content of H_2O in MIs was studied with ionic probe. Water concentrations in MIs ranging from 0.07 to 0.29 wt.% are close to those in Nauru basaltic glasses and melt microinclusions reported in (Simonov et al., 2004), i.e. to normal dry magmas of N-MORB. In the La/Sm_N versus H_2O/Ce diagram MIs compositions plot in the field of Mid-Atlantic ridge glasses (Fig. 11, *B*) (Michael, 1995; Simonov et al, 2004).
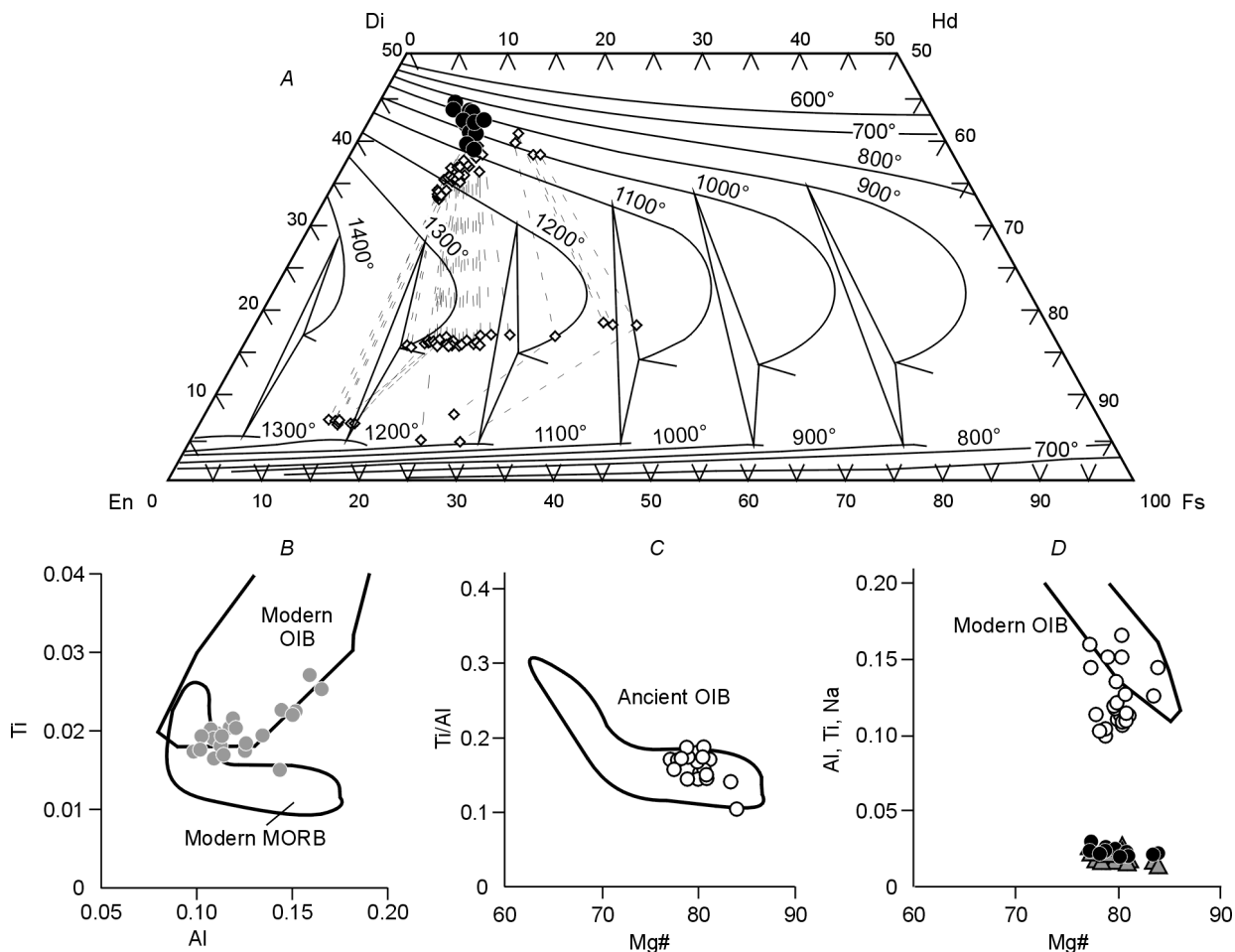
Fig. 10. Compositions of relict igneous clinopyroxene from enriched basalt C-80A-04 on Lindsley's (1983) quadrilateral diagram (*A*), *B* — binary plot of Al vs. Ti (atoms p.f.u. based on 6 oxygens). *C* — binary plot Mg# vs. Ti/Al. *D* — combined binary plots Mg# vs. Ti (triangles), Al (open circles), Na (filled circles). Field boundaries were borrowed from (Komiya et al., 2002).
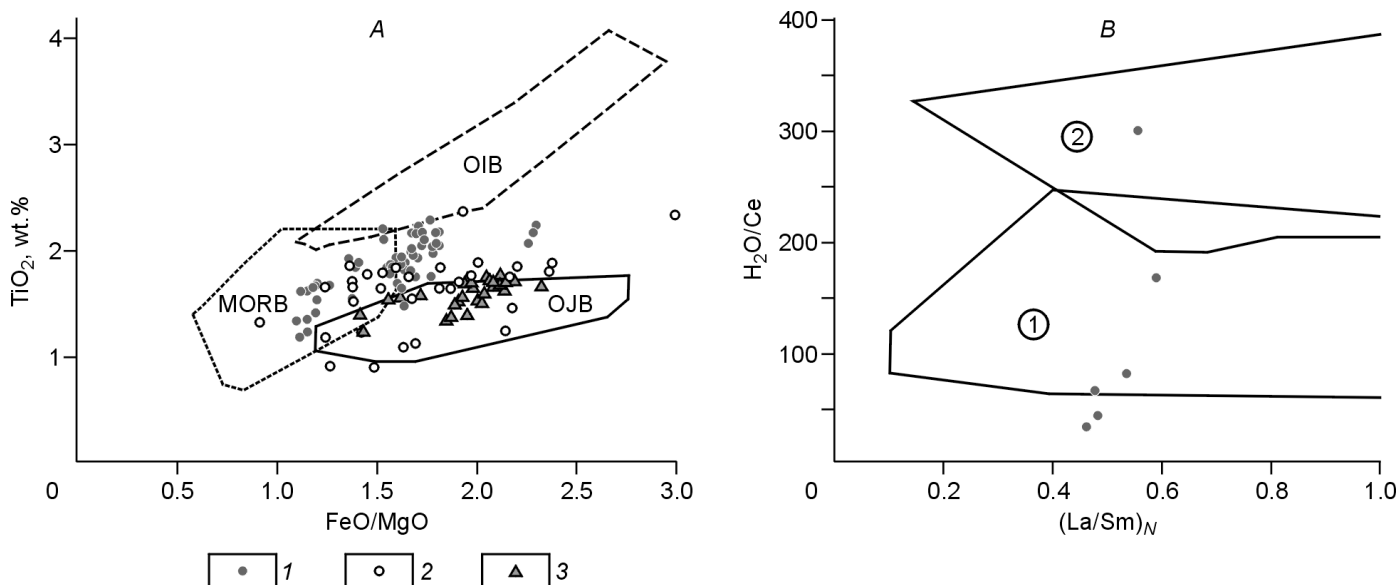
Fig. 11. Composition of melt microinclusions compared with whole rock basalt and volcanic glass. *A* — binary plot TiO$_2$ vs. FeO/MgO. *1, 3* — clinopyroxene-hosted homogenized melt microinclusions, Kurai accretionary belt (*1*) and Nauru Basin (*3*); *2* — Baratal paleoseamount whole rock data. OJB — Ontong-Java plateau basalts. *B* — binary plot H$_2$O/Ce vs. (La/Sm)$_N$ for clinopyroxene-hosted melt microinclusions, Kurai accretionary belt. Fields: 1 — Mid-Atlantic Ridge volcanic glass sampled north of 35° N; 2 — mid-oceanic ridge and intraplate basalt glasses sampled in the Pacific and Indian Ocean modified from (Simonov et al., 2004) and (Michael, 1995).

Possible effects of secondary alteration, metamorphism, crustal contamination and fractional crystallization

It is a common knowledge that basalts formed in different geodynamic settings have different compositions, therefore the basaltic units incorporated in accretionary belts hold key information for reconstructing their origin and tectonic evolution. In general, initial composition of volcanic mafic complexes depends on depth/type of mantle source, degree of partial melting, fractional crystallization and contamination of basaltic melts by sialic (continental) and/or mafic (oceanic) crust. However, after lava is erupted on the surface or oceanic floor its composition can be affected by various post-magmatic processes, such as sea-floor hydrothermal alteration and metamorphism, greenschist metamorphism, surface weathering, etc. Therefore, we must evaluate a degree of the change of initial composition of basalts by post-magmatic processes before interpreting their geochemical data and reconstructing their geodynamic history.

Secondary alteration and metamorphism. Variable mobility of element is quite possible in Vendian volcanic rocks that have undergone seafloor hydrothermal alteration, greenschist to amphibolite facies metamorphism, and tectonic deformation. Nevertheless, there is general agreement that REE, HFSE, and some transition metals are least sensitive to mobility (e.g. Condie, 1994; Ludden et al., 1982; Winchester and Floyd, 1977). Evidence for low mobility of HFSE, REE (except Eu) and, to a lesser degree, Th include the following: (1) there is no significant enrichment or depletion of groups of elements (e.g. LREE) in a given rock type over a range of LOI; (2) REE and primitive mantle-normalized trace element diagrams of given suites of basalts associated in the field exhibit coherent patterns for Th, HFSE, and REE (Fig. 8, 9); (3) Th/La$_{pm}$ and Nb/La$_{pm}$ do not correlate with the CIA (chemical index of alteration), Eu/Eu*, or loss on ignition (Fig. 12).

An additional source of information about primary magma composition is composition of melt microinclusions in phenocrysts of porphyric varieties of mafic igneous rocks. The geodynamic and petrogenetic reconstructions did not take into account samples with high LOI and profound Eu anomalies as well as concentrations of Na, K, Ba, Rb, and Sr — elements mobile during post-magmatic processes.

Contamination by continental crust is quite possible, though numerous lines of geological evidence, provided by many geologists previously worked in that region, are consistent with an intraoceanic setting for the basalt sequences (Berzin et al., 1994; Buslov et al., 1993, 2002; Dobretsov et al., 1992, 2004; Gibsher et al., 1996; Gusev, 1991; Simonov et al., 1994). The presence of chert and siliceous mudstone within tholeiitic pillowed basalts and flows and association of basalts with massive limestone suggest a marine environment rather than a continental setting for the eruption of the volcanic rocks.

Negative Nb anomalies in most basalts could possibly reflect some crustal contamination (Fig. 9), but, (1) Nb/La$_{pm}$

do not correlate with Th/La$_{pm}$; (2) Th contents are rather low (Table 1, Fig. 9, *A*); (3) geology-lithology relationships show that the basaltic units formed over the oceanic, not continental, lithosphere (see above).

A good example of crustally contaminated basalts is the Wawa greenstone belt of the Archean Yilgarn Craton, western Australia, and the Early Proterozoic Vetreny belt, Baltic Shield, where lavas were erupted through an older sialic basement (Arndt and Jenner, 1986; Redman and Keays, 1985). In those old basalts SiO$_2$, Th and LREE contents correlate with the magnitude of negative Nb anomalies, which is, however, not typical of the Kurai volcanic rocks (Fig. 13, *C*, *D*). In the diagrams compiled for the Vetreny belt (Puchtel et al., 1997) the Kurai lavas plot separately from those contaminated volcanic rocks (Fig. 13, *A–C*).

Thus, low Nb/La$_{pm}$ values do not result from contamination of tholeiitic liquids by continental crust during eruption (exogeneous contamination), but may have resulted from recycling of lithosphere into the mantle during subduction of the oceanic slab (endogenous contamination). The low concentrations of Th (0.3 ppm on average) also rule out crustal contamination (Table 1) (Li et al., 2002). The increased Th contents in three samples of the Kurai accretionary belt (Th/La$_{pm}$ > 1; samples 147, KR-86, KR-90) can be interpreted as a result of secondary alteration.

Fractional crystallization. The variation of MgO in all varieties of basalts is great enough to suggest a fractional crystallization control on Nb anomalies because Nb is compatible in Fe-Ti oxides, which are likely to be fractionating phases (Table 1, Fig. 7). The limited variation of La/Sm$_N$ ratios in the depleted and most transitional basalts over a wide range of Mg# (from 30 to 60) suggest that there was no significant LREE fractionation as a result of fractional crystallization of clinopyroxene, and there is no correlation of Nb anomalies with Mg# as well (Fig. 13, *E*). On the other hand, Fe–Ti oxides may accommodate Nb, yet there is no correlation of Nb/La$_{pm}$ with Ti/Ti* (Fig. 13, *F*), therefore Nb fractionation by Fe-Ti oxides cannot be regarded a factor of Nb redistribution after the formation of initial basaltic melts. None of the basalt groups shows any correlation between Fe$_2$O$_3$ and ratios Nb/La$_{pm}$ and Th/La$_{pm}$. Consequently, Th-Nb-LREE interelement ratios in the volcanic rocks are rather independent of clinopyroxene and Fe-Ti oxide fractional crystallization (Fowler and Jensen, 1989; Polat et al., 1999). Chromium depletion in most transitional samples suggests fractionation of Cr-spinels in intermediate chambers (Table 1, Fig. 7).

Mantle sources and petrogenesis

Melting processes. Variable compositions of major and trace elements in the Kurai lavas suggest different degree of partial melting. Negative Nb anomalies with respect to La and Th are typical of both depleted and transitional basalt varieties (Figs. 9, *A*, 13). For example, Bach et al. (1996) attributed the Nb depletions to second stage melting of a mantle source that had experienced previous melt extraction under extremely low
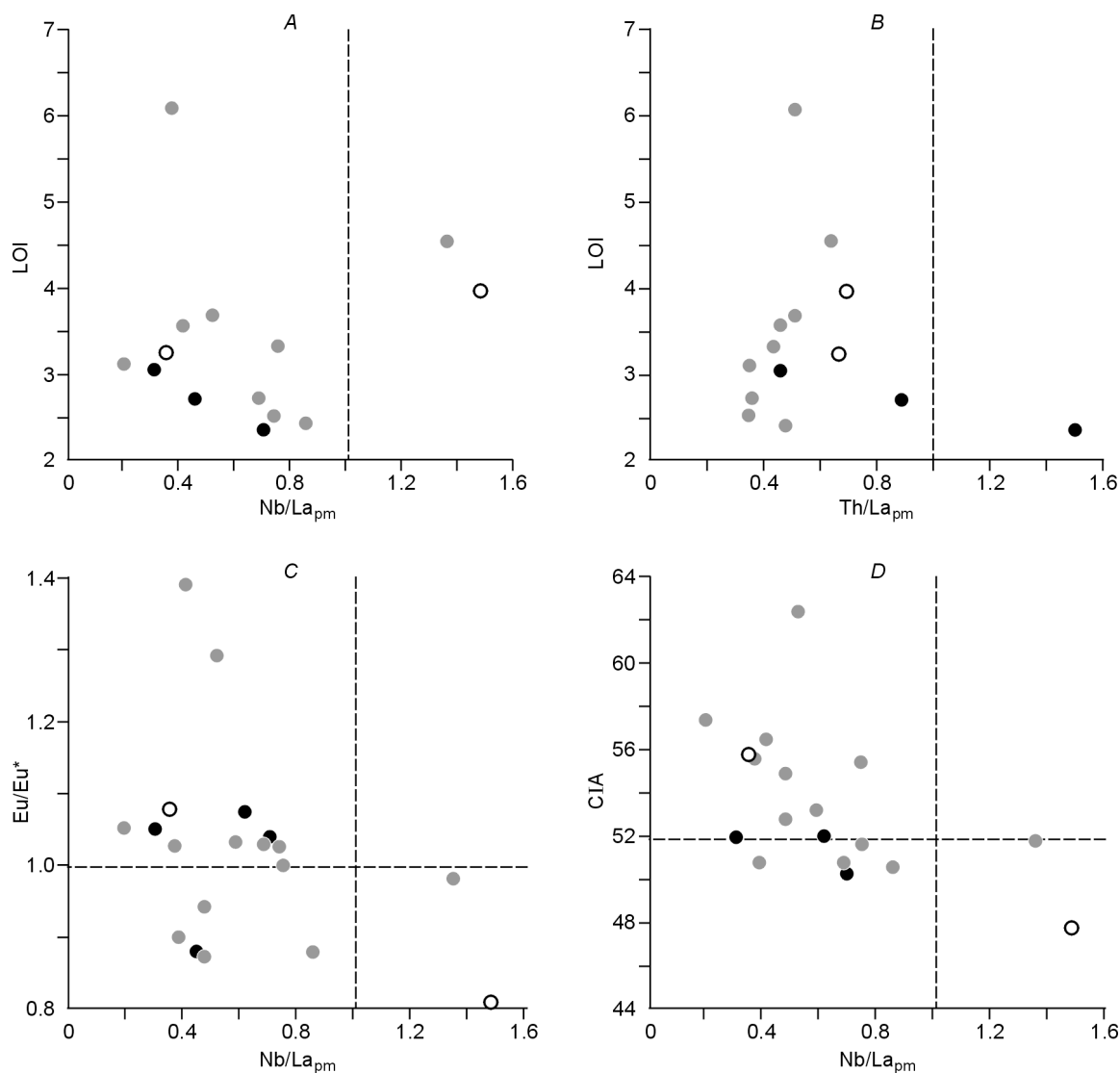
Fig. 12. Loss on ignition (LOI) vs. Nb/La$_{pm}$ (*A*) and Th/La$_{pm}$ (*B*), Eu/Eu* versus Nb/La$_{pm}$ (*C*) and chemical index of alteration (CIA) vs. Nb/La$_{pm}$ (*D*) (Nesbitt and Young, 1982) (CIA = Al$_2$O$_3$/(CaO + Na$_2$O + K$_2$O + Al$_2$O$_3$)) for the three basalt varieties, indicating that Th-Nb-La interelement ratios do not correlate with alteration and metamorphism. The dashed lines are primitive mantle ratios, from (Sun and McDonough, 1989). Symbols as in Fig. 4.

degrees of partial melting. However, thorium depletion should occur along with Nb depletion during low degrees of partial melting, but this is not consistently seen in the most of Kurai tholeiites (Th = 0.15–0.8 ppm). On the other hand, the partial melting could be admitted at a depth of the spinel facies because most depleted and transitional basalts have non-fractionated HREE (Fig. 8). However, there is no correlation of Nb/La$_{pm}$ or Th/La$_{pm}$ with Gd/Yb$_N$, which is characteristic of rocks formed as a result of partial melting, and samples with fractionated HREE may have both positive and negative Nb anomalies (Table 1).

Mantle sources. Based on the above argumentation we suggest that secondary alteration and metamorphism, crustal assimilation, fractional crystallization and mantle melting can all be ruled out as the cause of variations in the Th-Nb-LREE systematics. Then, those variations may be a signature of compositionally heterogeneous mantle (Polat et al., 1999).

As far as Nb, La and Th have similar partition coefficients, they are unlikely to be fractionated from one another during the relatively high-degree partial melting involved in the genesis of ultramafic and mafic oceanic lavas (Sun and McDonough, 1989). Saunders et al. (1988) demonstrated that the Th-Nb-Ce systematics of oceanic basalts can be described in terms of mixing between three mantle components: (1) DMM — depleted MORB source mantle (DMM) with relatively high Ce/Nb but low Th/Nb; (2) RSC — a recycled residual slab component processes through a subduction zone having low Ce/Nb and Th/Nb; (3) SDC — a recycled subduction-derived component with high Th/Nb and Ce/Nb, i.e. complementary to RSC (Fig. 14). During subduction Th and LREE are fractionated from Nb: the former elements are preferentially transferred to the subarc mantle from the slab whereas Nb is not, and later are involved into island-arc volcanism. The residual slab — RSC — hosts more inert Nb and has a positive Nb anomaly relative to Th and LREE.
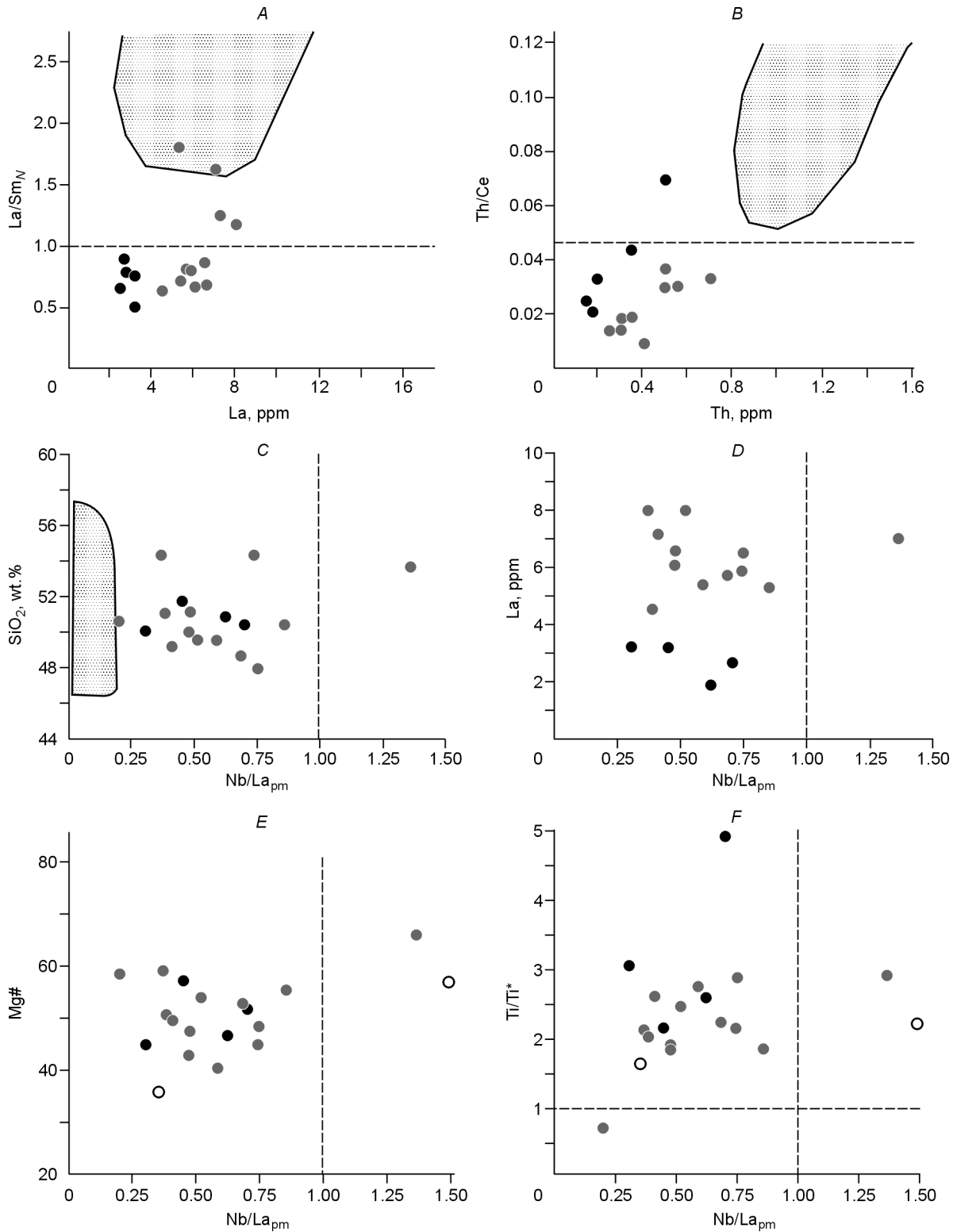
Fig. 13. Plots of La vs. La/Sm$_N$ (*A*), Th vs. Th/Ce (*B*), Nb/La$_{pm}$ vs. SiO$_2$ (*C*) and Nb/La$_{pm}$ vs. La (*D*) for depleted and transitional basalt varieties and plots Nb/La$_{pm}$ vs. Mg# (*E*) and Nb/La$_{pm}$ vs. Ti/Ti*(*F*) for all groups of basalts indicating that crustal contamination (*A–D*) and fractional crystallization (*E–F*) did not influence the Th–Nb–La systematics. The dashed lines are primitive mantle ratios, from (Sun and McDonough, 1989). Shaded areas (*A–C*) represent crustally contaminated lavas from the Vetreny belt, Baltic Shield (Puchtel et al., 1997). Symbols as in Fig. 4.

Consequently, the subarc mantle acquires a complementary negative Nb anomaly (SDC). The recycling, i.e. return of the oceanic crust back into the mantle, may occur by subduction and/or delamination.

Relatively low Nb/La$_{pm}$ are typical of most basalts of the Kurai accretionary belt (Table 1, Fig. 9) and may be attributed to the subduction-derived component SDC (Sun and McDonough, 1989; Weaver, 1991), however, in that case
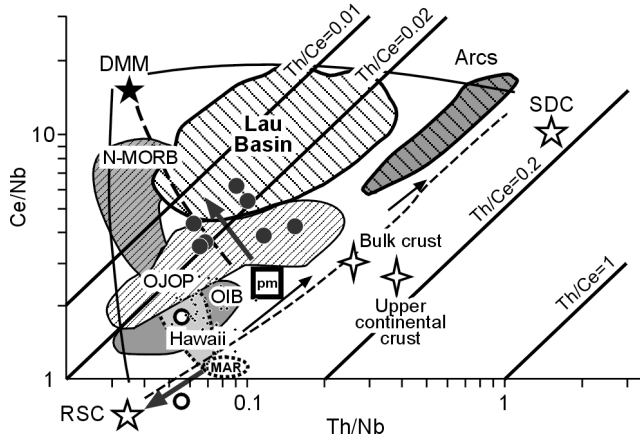
Fig. 14. Ce/Nb vs. Th/Nb variation diagram after (Saunders et al., 1988). Solid lines represent the simple mixing relations between depleted mantle (DMM), residue slab component (RSC) and slab derived component (SDC). Dashed lines indicate simple melt extraction path and origin of DMM, RSC and SDC (Polat et al., 1999). Thick arrows show paths for the mixing of RSC, DMM and pm (primitive mantle) for transitional (gray circles) and enriched (white circles) basalts of the Kurai accretionary belt. Fields for Nauru basin, Ontong Java oceanic plateau (OJOP) and Lau back-arc basin are from (Floyd, 1989), (Hemmond et al., 1993) and (Ewart et al., 1994), respectively. Data for Mid-Atlantic ridge (MAR) and island arcs are from (Saunders et al., 1988; 1991), respectively. Data for N-MORB, OIB, MORB, and pm are from (Sun and McDonough, 1989). Bulk continental crust values after Taylor and McLennan (1985). Field for Hawaii is based on the Geochemical Rock Database (GEOROC) of the Max-Planck-Institute for Chemistry in Mainz, Germany (www.georoc.mpch-mainz.gwdg.de/georoc).

Th/Nb_{pm} ratios also must be relatively high and exceed Nb/La_{pm}, which is not observed in the most of the basalts under investigation (Fig. 9, Table 1). Consequently, the participation of SDC component in the melting is beyond our consideration, and we interpret the low Nb/La_{pm} ratios as a result of the mixing of RSC and DMM-derived components. The rare samples, which have negative Nb and positive Th anomalies (nos. KR86, 147; Table 1), may carry material produced by post-magmatic alteration and, therefore, are not shown in the diagrams used for characterization of mantle sources.

Enriched basalts C-80A-04 and 123 have strong positive Nb anomalies relative to La and are likely formed with participation of recycled oceanic crust material, i.e. RSC component (Sun and McDonough, 1989; Weaver, 1991). Thus, as far as we know this is the first time that plume-related basalts have been identified in the Kurai accretionary wedge with a clear positive Nb, HIMU-like trace element signature ($Nb/La_{pm} > 1$; Figs. 9, 14) (Hofmann, 1997). This conclusion may or may not be supported by future Pb isotopic study. In the Th/Nb versus Ce/Nb diagram (Fig. 14) the transitional basalts of the Kurai belt plot in the Ontong-Java field.

Many authors have shown that the Cretaceous to Quaternary plume-related oceanic plateau and island basalts, e.g. Ontong Java, Hawaii, Iceland, etc., have diverse geochemical compositions and several mantle components (Hards et al., 1995; Mahoney et al., 1993; Neal et al., 1997; Regelous et al., 2003). Oceanic basalts of the Baratal paleoseamount hosted by the Kurai accretionary wedge are characterized by

a wide range of trace elements (Th, HFSE, REE), suggesting their formation from several mixed mantle components. The Th/Nb versus Ce/Nb diagram (Fig. 14) shows that the depleted basalts could have been formed under participation of DMM and primitive mantle material. The enriched basalts possibly formed from a melt containing Nb-rich RSC and OIB-type components, which could be similar to that produced by the Hawaiian hot spot.

***PT*-conditions.** Crystallization temperature and pressure were estimated from the composition of clinopyroxene phenocrysts and in the experiments on homogenization of clinopyroxene-hosted melt inclusions.

Clinopyroxene compositions plotted on the Lindsley diagram (Fig. 10, *A*) show the temperatures of Cpx crystallization ranging from 1100 to 900 °C (Lindsley, 1983), which is slightly below the temperatures of crystallization calculated with mineral thermometers. Temperature estimates (Cpx thermometers) obtained using a special program written by Dr. Igor Aschepkov (personal communication) range from 1100 to 1295 °C (Mercier, 1981) and from 1008 to 1126 °C (Nimis and Taylor, 2000) at a fixed pressure of 2 kbar, which is a probable pressure in a shallow intermediate magmatic chamber. The obtained estimates accord well with homogenization temperatures of melt MIs — 1160–1190 °C (see section "Melt microinclusions hosted by clinopyroxene").

Liquidus temperatures were estimated with the help of PETROLOG software (Danyushevsky, 2001) from MIs compositions. The temperatures estimated for 1 kbar appeared to be close to the temperatures of homogenization, i.e. 1160–1190 °C (Fig. 15). Several liquidus estimates are above the homogenization temperatures, which suggests an increased content of water in the melt (Sobolev, 1997) roughly equivalent to 1 wt.% of H_2O, although the ion microprobe data show low to moderate H_2O contents in MIs ranging from 0.1 to 0.3 wt.% (Simonov et al., 2005) (Fig. 11, *B*). Thus, the study of pyroxenes and their hosted melt inclusions showed that the Kurai basaltic lavas were crystallized within a temperature range from 1160 to 1190 °C, which is similar to the data on pyroxene hosted melt inclusions of Nauru plateau basalts (Simonov et al., 2004).

Geodynamic settings of basalt eruption

At present, geochemical data are widely used for reconstructing geodynamic settings of magmatism. For each specific setting geological evidence should be taken into account, although original stratigraphic relations of volcanogenic and sedimentary rocks found in Precambrian and Paleozoic foldbelts are often disrupted and complicated by multi-phase deformation related to subsequent accretion and collision events. Nevertheless, in the Kurai accretionary belt basalts have primary relations with seamount carbonate "cap" and slope facies, and oceanic floor basalts have direct contacts with seamount slope facies and foothill sediments (Buslov et al., 1993; Dobretsov et al., 2004; Safonova et al., 2004; Uchio et al., 2004).
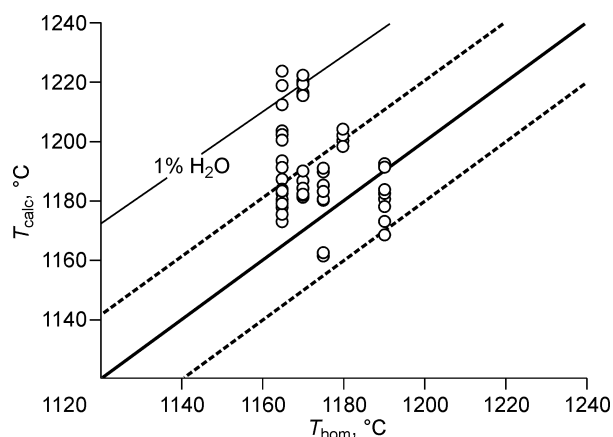
Fig. 15. Homogenization temperatures of melt microinclusions (T_{hom}) compared with the temperatures estimated from composition of microinclusions by PETROLOG software (Danyushevsky, 2001) for a pressure of 1 kbar.

Table 2 shows the criteria we used for reconstructing the geodynamic settings of the above mentioned groups of basalts. On the basis of the geological data and geochemical features, we can conclude that the oceanic basalts hosted by the Kurai accretionary belt were formed in the following geodynamic settings.

The depleted basalts of N-MORB geochemical type were formed in mid-oceanic ridge setting. Evidence for this comes from their association with pelagic, thin-bedded terrigenous siliceous sediments, occurrence of the dike complex, low TiO_2 contents, LREE depleted rare-earth patterns and Nb depleted trace element diagrams (Table 1, Fig. 9).

The enriched basalts of OIB geochemical type were formed in oceanic island setting and are characterized by close association with siliceous-carbonate clastic slope facies and enrichment in Ti, LREE and Nb ($Nb/La_{pm} > 1$). This suggests the presence of RSC in the mantle source and the spinel-facies depth of partial melting ($Gd/Yb_N = 1–1.5$) (Table 1, Figs. 9, 10, 14).

The transitional basalts of OPB type are geochemically close to Western Pacific plateau basalts and were formed either in seamount setting, similar to that of the Emperor Seamount Chain (Regelous et al., 2003), or in a setting of combined oceanic island and oceanic plateau, as in the Ontong-Java plateau (Neal et al., 1997). The evidence comes from their association with slope facies sediments, presence of an up to 500 m thick carbonate "cap" overlapping the basalts (Uchio et al., 2004) and specific geochemical features: medium concentrations of TiO_2 (1.7 wt.% average), flat REE patterns and negative Nb anomalies relative to La. However, the transitional basalts, unlike their suprasubduction counterparts, are not characterized by increased Th, i.e. in most samples $Nb/La_{pm} > Th/La_{pm}$ and $Th/La_{pm} < 1$.

Conclusions

The performed study of the geological position and geochemical features of Paleo-Asian Ocean basalts, which presently occur as tectonic fragments incorporated in the Kurai accretionary belt, allowed the following conclusions:.

1. Titanium, Nb and LREE depleted, transitional and enriched basalts coexist. The depleted varieties are compositionally close to N-MORB and are associated with thin-bedded siliceous sediments. The transitional and enriched varieties are similar to Pacific intraplate basalts and associated with carbonate-siliceous (slope facies) and carbonate "cap" (oceanic island/seamount) sediments.

2. The geochemical features indicate that the N-MORB basalts were derived from a depleted upper mantle source (DMM), whereas the transitional and enriched basalts formed from a heterogeneous mantle source including both DMM and RSC components.

3. The temperature estimates for basalts, obtained by the composition of pyroxene phenocrysts and experiments on

Table 2

Characteristic geochemical and geological features of Kurai basalts from different geodynamic settings: mid-oceanic ridge (N-MORB), oceanic plateau (OPB) and oceanic island (OIB)

Basalts, TiO_2	REE patterns	(La/Sm$_N$)	Nb/La$_{pm}$	Th/La$_{pm}$	Zr/Nb	Geological assemblages	Conclusion
Depleted	1.21	LREE-depleted (0.57–0.89)	0.62	0.71	65	Associated thin-bedded chert; dike complex	MORB
Transitional	1.7	Mostly flat (0.7–1.63)	0.56	0.51	35	Associated carbonate-siliceous slope facies and "carbonate cap" limestone, tephra	OPB, OIB
Enriched	1.68	LREE-enriched (2.09–2.24)	0.8	0.68	26		
Normal mid-oceanic ridge basalts	1.2	LREE-depleted (0.6)	0.9	0.39	32	Associated pelagic sediments	—
Ontong-Java and Nauru plateau basalts	1.39	Mostly flat	1.0	0.7	17	Associated shallow-water (neritic) sediments	—
Oceanic island basalts	2.86	LREE-enriched (2.33)	1.25	0.87	6	Associated shallow-water slope facies and "carbonate cap" sediments	—

Note. Compiled using the data from (Frolova and Burikova, 2002) and (Kerr et al., 2000). Geochemical data for N-MORB, OIB and OPB are from (Sun and McDonough, 1989) and GEOROC database.

homogenization of clinopyroxene hosted melt microinclusions, are 1100–1295 °C and 1160–1190 °C, respectively.

4. The basalts formed in mid-oceanic ridge, oceanic island and oceanic plateau settings. The evidence for oceanic island and plateaus, which probably existed in the Paleo-Asian Ocean, comes from the close relationship between plume-related and oceanic floor basalts. Our data suggest that the Paleo-Asian Ocean evolved similarly to the Pacific Ocean, i.e. there acted Hawaiian-type hot spots and large mantle plumes which formed basaltic plateaus like that of Ontong-Java.

Acknowledgements

References

Arndt, N.T., Jenner, G.A., 1986. Crustally contaminated komatiites and basalts from Kambalda, Western Australia. Chemical Geology 56, 229–255.

Bach, W., Erzinger, J., Dosso, L., Bollinger, C., Bougnault, H., Etoubleau, J., Sauerwein, J., 1996. Unusually large Nb-Ta depletion in North Chile ridge basalts at 36°50″ to 38°56″ S: major element, trace element, and isotopic data. Earth Planetary Sci. Lett. 142, 223–240.

Berzin, N.A., Coleman, R.G., Dobretsov, N.L., Zonenshain, L.P., Xiao Xuchang, Chang, E.Z., 1994. Geodynamic map of the western part of the Paleoasian Ocean. Geologiya i Geofizika (Russian Geology and Geophysics), 35 (7–8), 8–28 (5–22).

Berzin, N.A., Kungurtsev, L.V., 1996. Geodynamic interpretation of Altai-Sayan geological complexes, Geologiya i Geofizika (Russian Geology and Geophysics) 37 (1), 63–81 (56–74).

Bobrov, V.A., Kalugin, I.A., Phedorin, M.A., 1998. SR XFA of element composition of bottom sediments from Teletskoye Lake. Nuclear instruments and methods in physics research, A405, 569–571.

Buslov, M.M., Berzin, N.A., Dobretsov, N.L., Simonov, V.A., 1993. Geology and Tectonics of Gorny Altai. UIGGM Publ., Novosibirsk.

Buslov, M.M., Saphonova, I.Yu, Watanabe, T., Obut, O. T., Fujiwara, Y., Iwata, K., Semakov, N.N., Sugai, Y., Smirnova, L.V., Kazansky, A.Yu., Itaya, T. 2001. Evolution of the Paleo-Asian Ocean (Altai-Sayan Region, Central Asia) and collision of possible Gondwana-derived terranes with the southern marginal part of the Siberian continent. Geoscience J. 5 (3), 203–224.

Buslov, M.M., Watanabe, T., 1996. Intrasubduction collision and its role in the evolution of an accretionary wedge: the Kurai zone of Gorny Altai, Central Asia. Geologiya i Geofizika (Russian Geology and Geophysics) 37 (1), 82–93 (83–94).

Buslov, M.M., Watanabe, T., Saphonova, I.Yu., Iwata, K., Travin, A., Akiyama, M., 2002. Vendian-Cambrian island arc system of the Siberian continent in Gorny Altai (Russia, Central Asia). Gondwana Res. 5 (4), 781–800.

Condie, K.C., 1994. Greenstones through time, in: K.C. Condie (Ed.) Archean Crustal Evolution. Amsterdam, Elsevier, pp. 85–120.

Danyushevsky, L.V., 2001. The effect of small amounts of H_2O on crystallisation of mid-ocean ridge and backarc basin magmas. J. Volcan. Geoth. Res. 110, (3–4), 265–280.

Dobretsov, N.L., Zonenshain, L.P. (Eds.), 1985. Riphean-Paleozoic Ophiolites of North Eurasia [in Russian]. Nauka, Novosibirsk.

Dobretsov, N.L., Berzin, N.A., Buslov, M.M., Ermikov, V.D., 1995. General aspects of the evolution of the Altai region and in interrelationships between its basement pattern and the neotectonic structural development. Geologiya i Geofizika (Russian Geology and Geophysics) 36 (10), 5–20 (3–16).

Dobretsov, N.L., Buslov, M.M., Safonova, I.Yu., Kokh, D.A., 2004. Fragments of oceanic islands in the Kurai and Katun accretionary wedges of Gorny Altai. Geologiya i Geofizika (Russian Geology and Geophysics) 45 (12), 1381–1403 (1325–1348).

Dobretsov, N.L., Simonov, V.A., Buslov, M.M., Kurenkov, S.A., 1992. Oceanic and island-arc ophiolites of Gorny Altai. Geologiya i Geofizika (Russian Geology and Geophysics) 12, 3–14 (1–12).

Ewart, A., Hergt J.M., Hawkins, J.M., 1994. Major element, trace element, and isotope (Pb, Sr, Nd) geochemistry of site 839 basalts and basaltic andesites, implications for arc volcanism. Proc. Ocean Drilling Program, Sci. Results 135, 519–531.

Floyd, P.A., 1989. Geochemical features of intraplate oceanic plateau basalts, in: Saunders, A.D., Norry, M.J. (Eds.), Magmatism in the Ocean Basins. Geol. Soc., Spec. Publ. 42. London, pp. 215–230.

Fowler, A.D., Jensen, L.S., 1989. Quantitative trace element modeling of the crystallization history of the Sinojevis and Blake River groups, Abitibi greenstone belt, Ontario. Can. J. Earth Sci. 26, 1356–1365.

Frolova, T.I., Burikova, I.A., 1997. Magmatic Formations in Modern Geotectonic Environments [in Russian]. Moscow Univ. Press, Moscow.

Frolova, T.I., Burikova, I.A., 2002. Plateau-basaltic magmatism and ocean formation, in: Disputable Aspects of Plate Tectonics and Possible Alternatives [in Russian]. OIFZ RAN Publ., Moscow, pp. 30–48.

Gibsher, A.S., Esin, S.V., Izokh, A.E., Kireev, A.D., Petrova, T.V., 1997. Cambrian diopside-bearing basalts from the Cheposh zone in Gorny Altai. Geologiya i Geofizika (Russian Geology and Geophysics) 38 (11), 1760–1773 (1789–1801).

Gordienko, I.V., Filimonov, A.V., 2003. Magmatism, metamorphism and deformation of the lithosphere during the closure of the Paleo-Asian Ocean: implication from the study of the Paleozoic Dzhida zone of the Central-Asian foldbelt, unsolved problems, in: Proc. Sci. Conf. Inst. Geogr. Publ., Irkutsk, pp. 60–65.

Gusev, N.I., 1991. Reconstruction of geodynamic regimes for Precambrian and Cambrian volcanism in southeastern Gorny Altai, in: Kuznetsov, P.P., et al. (Eds.). Paleogeodynamics and Formation of Mineral-Rich Zones in South Siberia. OIGGM SO RAN SSSR, Novosibirsk, pp. 32–54 [in Russian].

Hards, V.L., Kempton, P.D., Thomson, R.N., 1995. The heterogeneous Iceland plume of the Snaefell volcanic centre. J. Geological Soc. London 152, 1003–1009.

Hemond, C., Arndt N.T., Lichtenstein, U., Hofmann, A.W., Oskarsson, N., Steinthorsson, S., 1993. The heterogeneous Iceland plume: Nd-Sr-O isotope and trace element constraints. J. Geophysics Res. 98, 15,833–15,850.

Hofmann, A.W., 1997. Mantle geochemistry: the message from oceanic volcanism. Nature, 385, 219–229.

Isozaki, Y., Maruyama, Sh., Fukuoka, F., 1990. Accreted oceanic materials in Japan. Tectonophysics 181, 179–205.

Jensen, L.S., 1976. A new cation plot for classifying subalkalic volcanic rocks. Ontario Division Mines Misc., 66.

Kerr, A.C., White, R.V., Saunders, A.D., 2000. LIP reading: Recognizing oceanic plateaus in the geological record. J. Petrology 41, 1041–1056.

Komiya, T., Maruyama, Sh., Hirata, T., Nohda, S., 2002. Petrology and geochemistry of MORB and OIB in the Mid-Archean North Pole region, Pilbara craton, Western Australia: Implications for the composition and temperature of the upper mantle at 3.5 Ga. Int. Geol. Rev. 44, 988–1016.

Kurenkov, S.A., Didenko, A.N., Simonov, V.A., 2002. Geodynamics of Paleospreading [in Russian]. Proc. GIN RAN. GEOS, Moscow, 294.

Lindsley, D.H., 1983. Pyroxene thermometry. American Mineralogist 68, 477–493.

Ludden, J., Gelinas, L., Trudel, P., 1982. Archean metavolcanics from the Rouyn-Noranda district, Abitibi greenstone belt, Quebec. 2. Mobility of trace elements and petrogenetic constrains. Can. J. Earth. Sci. 19, 2276–2287.

Mahoney, J.J., Storey, M., Duncan, R.A., Spencer, K.J., Pringle, M., 1993. Geochemistry and geochronology of Leg130 basement lavas: nature and origin of the Ontong Java Plateau, in: Proc. Ocean Drilling Program, Sci. Results 130, pp. 3–22.

Mercier, J.-C.C., 1981. Single-pyroxene thermobarometry. Tectonophysics 70, 1–37.

Michael, P.J., 1995. Regionally distinctive sources of depleted MORB: evidence from trace elements and H_2O. Earth Planet. Sci. Lett. 131, 301–320.

Miyashiro, A., 1973. The Troodos ophiolitic complex was probably formed in an island arc. Earth Planet. Sci. Lett. 19, 218–224.

Neal, C.R., Mahoney, J.J., Kroenke, L.W., Petterson, M.G., 1997. The Ontong Java Plateau. Large Igneous Provinces: continental, oceanic and planetary flood volcanism, in: Mahoney, J.J. (Ed.), Geophysical Monograph, American Geophysical Union, pp. 183–216.

Nesbitt, H.W., Young, G.M., 1982. Early Proterozoic climates and plate motions inferred from major element chemistry of lutites. Nature 299, 715–717.

Nimis, P., Taylor, W., 2000. Single clinopyroxene thermobarometry for garnet peridotites. Part 1. Calibration and testing of a Cr-in-Cpx barometer and an enstatite-in-Cpx thermometer. Contrib. Mineral. Petrol. 139, 541–554.

Nisbet, E.G., Pearce, J.A., 1977. Clinopyroxene composition in mafic lavas from different tectonic setting. Contrib. Mineral. Petrol. 63, 149–160.

Ota, T., Utsunomiya, A., Uchio, Yu., Isozaki, Y., Buslov, M., Ishikawa, A., Maruyama, Sh., Kitajima, K., Kaneko, Y., Yamamoto, H., Katayama, I., 2007. Geology of the Gorny Altai subduction-accretion complex, southern Siberia: Tectonic evolution of a Vendian-Cambrian intraoceanic arc. J. Asian Earth Sci. 30, 666–695.

Phedorin, M.A., Bobrov, V.A., Chebykin, E.P., Goldberg, E.L., Melgunov, M.S., Filipova, S.V., Zolotarev, K.V., 2000. Comparison of synchrotron radiation X-ray fluorescense with conventional techniques for the analysis of sedimentary samples. Geostan. Newsletter 24 (2), 205–216.

Puchtel, I.S., Hasee, K.M., Hofmann, A.W., Chauvel, C., Kulikov, V.S., Garbe-Schonberg, C.-D., Nemchin, A.A., 1997. Petrology and geochemistry of crustally contaminated komatiitic basalts from the Vetreny belt, southeastern Baltic shield: evidence for an early Proterozoic mantle plume beneath rifted Archean continental lithosphere. Geochim. Cosmochim. Acta 61, 1205–1222.

Redman, I.S., Keays, R.R., 1985. Archean volcanism in the eastern Goldfields province, Western Australia. Precambrian Res. 30, 113 — 152.

Regelous, M., Hofmann, A.W., Abouchami, W, Galer, S.J.G., 2003. Geochemistry of lavas from the Emperor seamounts, and the geochemical evolution of Hawaiian magmatism from 85 to 42 Ma. J. Petrology 44 (1), 113–140.

Safonova, I.Yu., Buslov, M.M., 2004. Geochemistry of oceanic basalts of the Kurai accretionary prism (Gorny Altai), in: Vladykin, N.V. (Ed.), Deep-Seated Magmatism, Its Sources and Their Relation to Plume Processes [in Russian]. Vinogradov's Inst. Geochem. Publ., Irkutsk, pp. 314–332.

Safonova, I.Yu., Buslov, M.M., Iwata, K., Kokh, D.A., 2004. Fragments of Vendian-Early Carboniferous oceanic crust of the Paleo-Asian Ocean in foldbelts of the Altai-Sayan region of Central Asia: geochemistry, biostratigraphy and structural setting. Gondwana Res. 7 (3), 771–790.

Saunders, A.D., Norry, M.J., Tarney, J., 1988. Origin of MORB and chemically depleted mantle reservoirs: trace element constrains. J. Petrology. Spec. Lithosphere Iss., 415–455.

Saunders, A.D., Norry, M.J., Tarney, J., 1991. Fluid influence on the trace element compositions of the subduction zone magmas, in: Philos. Trans. Roy. Soc. London A., 335, pp. 337–392.

Simonov, V.A., 1993. Petrogenesis of Ophiolites (Thermobarogeochemical Research) [in Russian]. UIGGM SB RAS Publ., Novosibirsk.

Simonov, V.A., Dobretsov, N.L., Buslov, M.M., 1994. Boninite series in structures of the Paleoasian Ocean. Geologiya i Geofizika (Russian Geology and Geophysics) 35 (7–8), 182–199 (157–171).

Simonov, V.A., Safonova, I.Yu., Kovyazin, S.V., Buslov, M.M., 2005. Petrogenesis of basalts of the Kurai paleoseamount (Gorny Altai), in: Petrology of Magmatic and Metamorphic Complexes [in Russian] (5). TsNTI, Tomsk, pp. 130–135.

Simonov, V.A., Zolotukhin, V.V., Kovyazin, S.V., Al'mukhamedov, A.I., Medvedev, A.Ya., 2004. Petrogenesis of basaltic series of the Ontong Java-Nauru submarine plateau, Pacific Ocean [in Russian]. Petrologiya 12 (2), 191–205.

Sobolev, A.V., 1996. Melt inclusions in minerals as a source of principal petrological information. Petrologiya 4 (3), 228–239.

Sobolev, A.V., 1997. Problems of Formation and Evolution of Mantle Magmas. DSc Thesis [in Russian], Moscow.

Sobolev, A.V., Danyushevsky, L.V., 1994. Petrology and geochemistry of boninites from the north termination of the Tonga trench: constraints on the generation conditions of primary high-Ca boninite magmas. J. Petrology 35, 1183–1211.

Sun, S., McDonough, W.F., 1989. Chemical and isotopic systematics of oceanic basalts: Implications for mantle composition and processes. Magmatism in the Ocean Basins, in: Saunders, A.D., Norry, M.J. (Eds.), Geology Society London, Spec. Publ. 42, pp. 313–345.

Taylor, S.T., McLennan, S.M., 1985. The Continental Crust: Composition and Evolution. Blackwell, Oxford, 312.

Uchio, Yu., Isozaki, Yu., Ota, T., et al., 2004. The oldest mid-oceanic carbonate buildup complex: setting and lithofacies of the Vendian (Late Neoproterozoic) Baratal limestone in the Gorny Altai Mountains, Siberia. Proc. Japan Acad 80 (9), 422–428.

Watanabe, T., Buslov, M.M., Koitabashi, S., 1994. Comparison of arc-trench systems in the Early Paleozoic Gorny Altai and the Mesozoic-Cenozoic of Japan, in: Coleman, R.G. (Ed.) Reconstruction of the Paleo-Asian Ocean. VSP Int. Sci. Publ., The Netherlands, pp. 160–177.

Winchester, J.A., Floyd, P.A., 1977. Geochemical discrimination of different magma series and their differentiation products using immobile elements. Chem. Geol. 20, 325–343.

Zybin, V.A., Sergeev, V.P., 1978. Upper Paleozoic Stratigraphy of south-eastern Gorny Altai, in: News in Precambrian Stratigraphy and Paleontology of Altai-Sayan and Tuva [in Russian]. IGIG Publ., Novosibirsk, pp. 9–22.

Editorial responsibility: V.A. Vernikovsky